Thin–Walled Structures 192 (2023) 111048

Contents lists available at ScienceDirect

Thin-Walled Structures

journal homepage: www.elsevier.com/locate/tws

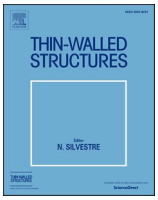

Full length article

Experimental investigation of the behaviour and capacity of sheathed cold-formed steel stud walls under inward flexural loading

Fatih Yilmaz [a,b], Jurgen Becque [c], Seyed Mohammad Mojtabaei [d,*], Iman Hajirasouliha [a]

[a] Department of Civil and Structural Engineering, The University of Sheffield, Sheffield S1 3JD, UK
[b] Department of Civil Engineering, Faculty of Engineering and Architecture, Recep Tayyip Erdogan University, Rize TR53100, Turkey
[c] Department of Engineering, University of Cambridge, Cambridge CB2 1PZ, UK
[d] School of Architecture, Building and Civil Engineering, Loughborough University, Leicestershire LE11 3TU, UK

ARTICLE INFO

Keywords:
Cold-Formed Steel (CFS)
Oriented Strand Board (OSB)
Experiment
Sheathed stud wall panel
Out-of-plane loading

ABSTRACT

A comprehensive experimental programme was designed and executed with the aim of investigating the out-of-plane bending behaviour and capacity of cold-formed steel (CFS) stud walls sheathed with wood-based boards. The influence of key design variables, including the screw spacing, the board material and thickness, the stud and track thicknesses, the board configuration (single-sheathed, double-sheathed and unsheathed) and the presence/absence of longitudinal seams, noggins and track sections, was investigated and quantified. A total of 15 stud walls sheathed with either Oriented Strand Board (OSB) or plywood were tested under four-point bending. Ancillary material tests, and push-out and pull-out connector tests were also performed. The results revealed a surprising richness in failure modes, given the initial geometric simplicity of the system. Simultaneous crushing of the OSB and distortional buckling failure of the studs, with either full or partial shear interaction, was a commonly observed failure mode. However, rotational and lateral–distortional deformations of the studs, often accompanied by longitudinal cracking of the boards, were also observed as a cause of failure.

1. Introduction

Cold-formed steel (CFS) members are widely used in the construction industry as both secondary and main load-carrying systems, as their application aligns well with the ever increasing importance of sustainability and cost-effectiveness. CFS provides many advantages compared to other structural materials, such as quick and straightforward installation, lightweight (facilitating transportation and handling), recyclability without loss of quality, and efficient material use. CFS stud walls are the key components in the construction of CFS buildings, where they are invariably clad with boards of various materials: cement board, OSB, plywood, etc. Their off-site manufacturing as panels allows unrivalled construction speeds, and 5–7 storey mid-rise buildings are achievable in non-seismic zones. Lateral stability is typically provided by strap bracing, although research has demonstrated that the sheathing contributes significant diaphragm stiffness in lateral in-plane loading scenarios [1–5]. It should be noted, however, that while CFS-framed buildings are gaining in popularity, some UK CFS fabricators report that as much as 95% of the stud walls they produce are used in applications which carry no vertical gravity loads, i.e. as either partition walls or 'curtain walls' around the building perimeter. In the latter case, the main loading on the stud walls originates from lateral wind loading on the building, which subjects the stud walls to either inward or outward flexure. Despite the importance in market share of this application, relatively few studies have been dedicated to the structural behaviour of sheathed CFS stud walls under flexural loading conditions, giving due consideration to the benefits of composite action between the CFS members and the boards.

In contrast, a rather large volume of previous research work is available on the in-plane shear behaviour of sheathed stud wall panels. While this topic is outside the scope of this paper, it is worth mentioning that the influence of various design parameters on their stiffness and capacity, including the loading conditions [6,7], the sheathing type and thickness [8–15], the screw behaviour [4,9,15–18] and the aspect ratio of the panel [7,19] has been extensively studied through experimental and numerical means.

With respect to the out-of-plane behaviour of sheathed CFS panels, Fiorino et al. [20] investigated seismic damage to non-structural partitions sheathed with gypsum-based boards. They conducted monotonic quasi-static and dynamic out-of-plane loading tests using a three-point

* Corresponding author.
E-mail address: smmojtabaei1@sheffield.ac.uk (S.M. Mojtabaei).

https://doi.org/10.1016/j.tws.2023.111048
Received 6 April 2023; Received in revised form 4 July 2023; Accepted 21 July 2023
Available online 12 September 2023

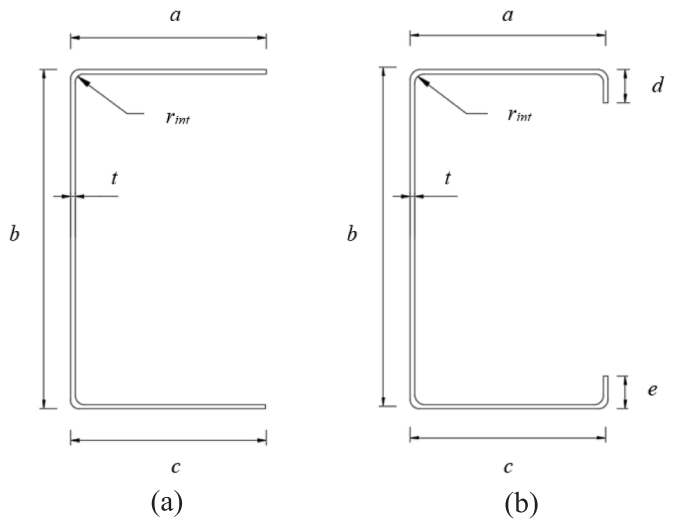

Fig. 1. Typical cross-sectional shapes and dimensional variables for: (a) track, (b) stud.

bending arrangement, while varying a range of design variables, including the wall height, the type of dowel connecting the track to the surrounding concrete structure (plastic or steel), the stud spacing, and the bottom connection between the studs and the track (i.e. a screwed connection or a non-screwed sliding connection). They observed that the strength and stiffness of the wall panels almost doubled by reducing the stud spacing from 600 mm to 300 mm. The post-peak response was significantly affected by the stud–track connection type, while the initial stiffness was influenced by both the dowel type and the stud–track connection. The type of dowel affected the ultimate strength of the system, but only in the case of a sliding bottom connection.

Mowrtage et al. [14] examined the out-of-plane bending capacity of CFS wall systems clad with steel sheets and shot-creted with cement or gypsum mortar. It was reported that the out-of-plane bending capacity of these wall panels was almost three times higher than the moment caused by the maximum wind pressure stipulated by the Turkish design code.

Selvaraj and Madhavan [21] conducted a comprehensive experimental investigation of CFS stud walls with double-sided gypsum boards under four-point bending. It was observed that the ultimate moment capacity of the sheathed system was increased by 126% compared to the unsheathed configuration, as a result of the restraining effect caused by the sheathing. It was also concluded that the AISI [22] design rules for the strength prediction of CFS flexural members with sheathing required modification. In a follow-up study, Selvaraj and Madhavan [23] assessed the bracing effect of gypsum sheathing in CFS stud wall panels through four-point bending tests on single studs, restrained on both sides by gypsum boards. It was shown that the effectiveness of the bracing depends on the global and local slenderness of the CFS stud. The experimental results also confirmed the adequacy of the fastener spacing limits contained in the AISI [22] guidelines for the case of CFS elements connected to gypsum boards. In another study by the same authors [24], the bracing effect of double-sided plywood sheathing in out-of-plane bending was examined as a function of the slenderness of the CFS stud. It was demonstrated that the effectiveness of the bracing mainly depends on the key parameters of the sheathing connection (i.e. the type of self-drilling screws) and the material properties of the board. It was also observed that the experimentally captured failure modes differed significantly from those predicted by the AISI S100 [25] design specifications.

It is evident from the literature that the connections between CFS framing members and the boards they are clad with play a fundamental role in the overall composite behaviour and the failure mechanism of the combined system. Various experimental and numerical studies have therefore been conducted on connection subassemblies to provide a better understanding of screwed connection behaviour. Ye et al. [26] tested sheathing-to-stud connections under monotonic and cyclic loading conditions while considering various sheathing materials, stud

Table 1
Parametric test matrix of CFS stud wall panels.

Parameters	Options	Specimen label	Width × Length (mm × mm)
Benchmark test	Key specimens	K1	1220 × 2440
		K2	1220 × 2440
Screw spacing	100 mm	S100	1220 × 2440
	150 mm	S150	1220 × 2440
	300 mm	S300	1220 × 2440
Materials and thicknesses	Plywood (9 mm)	P9	1220 × 2440
	OSB (18 mm)	OSB18	1220 × 2440
			1220 × 2440
	CFS (2 mm)	CFS2	
Sheathing configuration	Unsheathed	UB	1220 × 2440
	Double-Sided	DB1	1220 × 2440
		DB2	1220 × 2440
Stud spacing	305 mm	DR	610 × 2440
Secondary features	Seam	S	1220 × 2440
	Noggins	N	1220 × 2440
			1220 × 2440
	No track	NT	

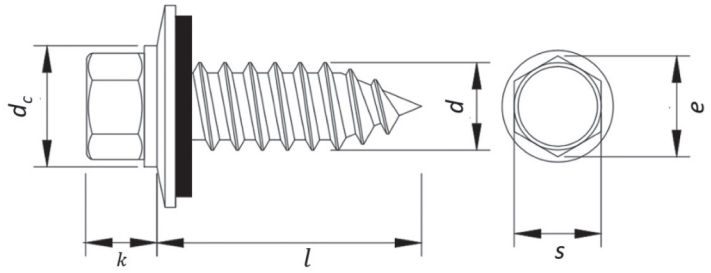

Diameter (*d*)	Hex Size (*s*)	Flange Diameter (d_c)	*k*	*e*	Length (*l*)
6.3 mm	8 mm	11 mm	5.45 mm	8.71 mm	25mm/45mm

Fig. 2. 6.3 mm diameter self-drilling screws with bonded washer.

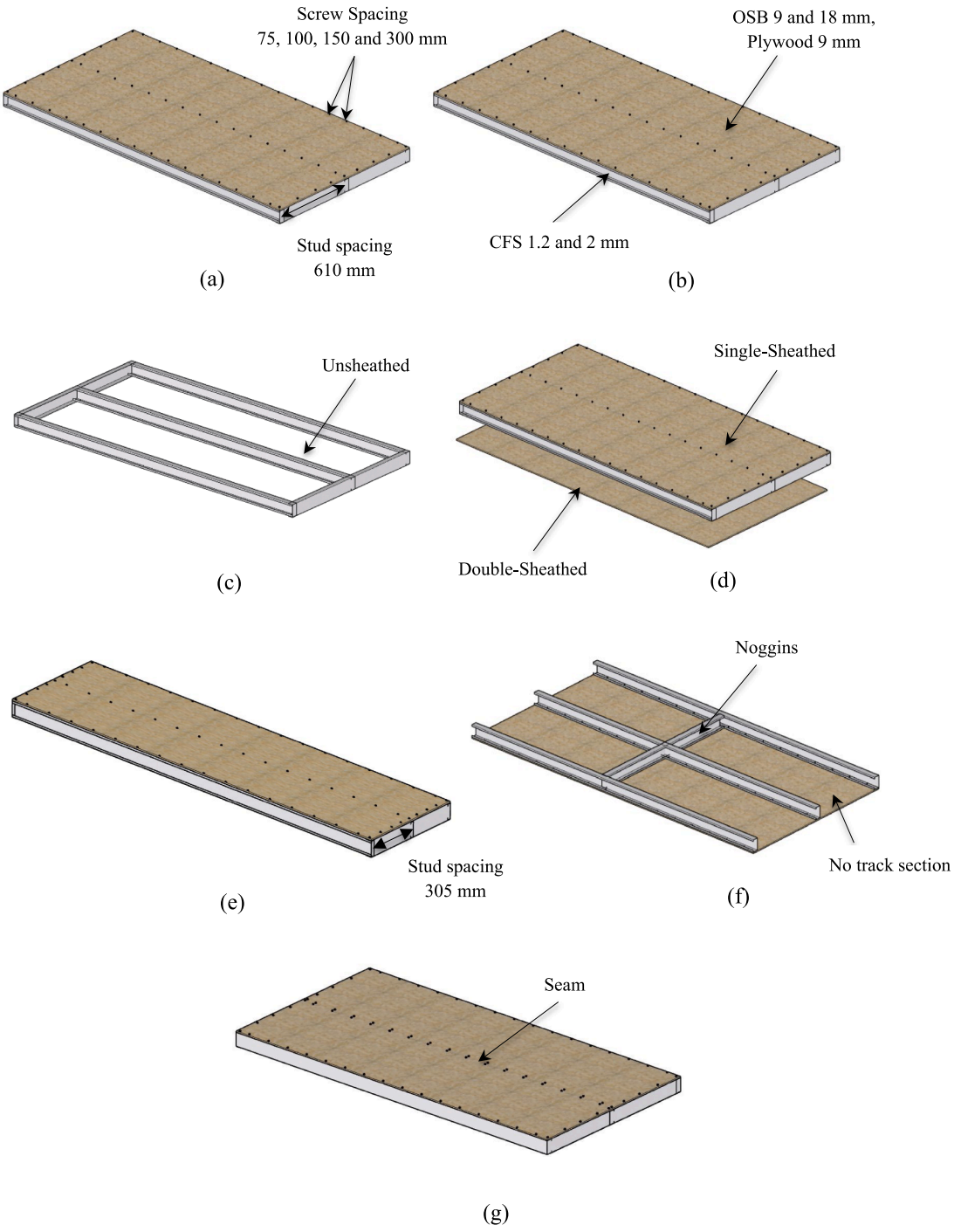

Fig. 3. Test specimen design parameters: (a) screw spacing, (b) material properties and thicknesses, (c, d) board configuration, (e) stud spacing and (f, g) presence/absence of seam, noggins and tracks.

Table 2
Average dimensions (out-to-out) of CFS framing members (in mm).

Specimen batch	t	r_{int}	Unlipped channel tracks			Lipped channel studs				
			a (flange)	b (web)	c (flange)	a (flange)	b (web)	c (flange)	d (lip)	e (lip)
1.2 mm CFS	1.19	2.8	57.57	99.66	57.43	50.57	99.73	50.64	8.93	11.11
2 mm CFS	1.92	3.2	56.76	103.20	57.38	49.19	100.64	49.31	13.93	15.16

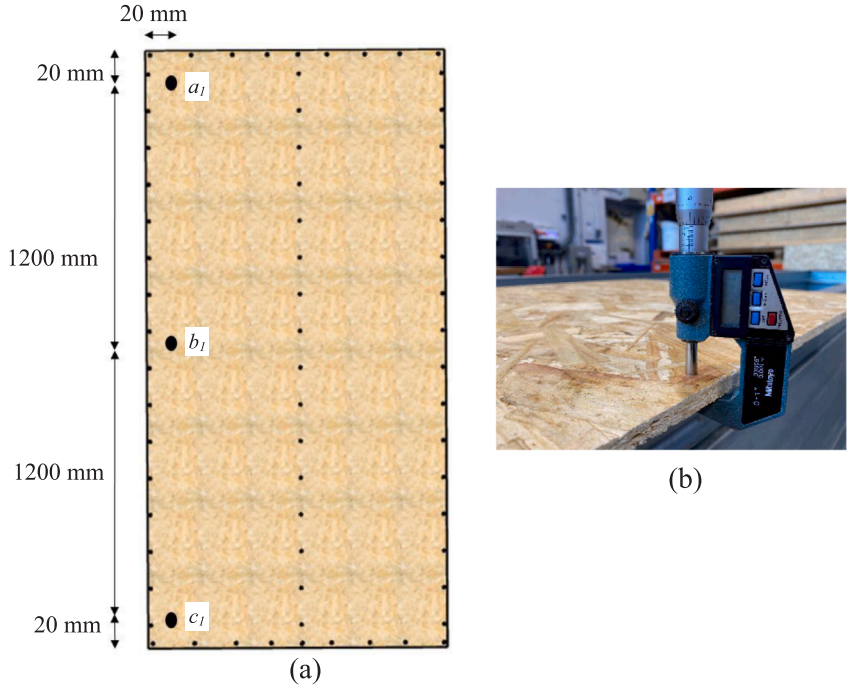

Fig. 4. (a) Locations of thickness measurements for wood-based boards, (b) micrometre.

Table 3
Average measured thickness of the tested wood-based boards.

Specimen batch	Thickness of the wood-based board (mm)			
	a_1	b_1	c_1	Average thickness
9 mm OSB	8.94	8.92	8.84	8.90
18 mm OSB	17.62	17.59	17.64	17.62
9 mm Plywood	9.66	9.59	9.69	9.65

thicknesses, screw diameters, edge distances and sheathing orientations. It was found that CFS panels with Calcium Silicate Board (CSB) sheathing experienced brittle damage (i.e. bursting of the sheathing edge), while a more ductile failure was observed in stud wall specimens sheathed with Oriented Strand Board (OSB), Gypsum Wall Board (GWB) and Bolivian Magnesium Board (BMG), caused by bearing failure, splitting of the sheathing, screw tilting/bending or shear failure of the screws. The results further demonstrated that, compared to the screw diameter and stud thickness, the edge distance has a much more noticeable effect on the connection capacity. Based on the results of the cyclic tests, the investigators also adopted a "four-line degradation" model [27] to fit the skeleton curves, and established the hysteretic characteristics of the connections using the "pivot" model [28].

Fiorino et al. [29] conducted a comprehensive experimental programme on CFS-to-gypsum board connections and CFS-to-cement-based board connections in order to assess the effects of panel type, thickness profile, screw diameter and number of panel layers. The connection

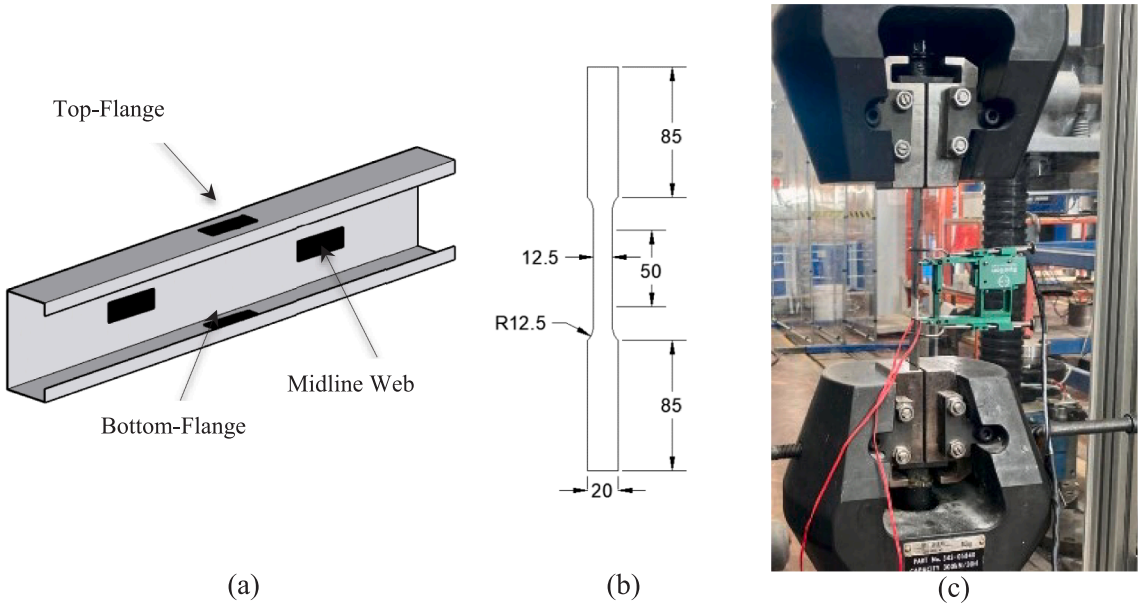

Fig. 5. (a) Sampling locations of CFS tensile coupons, (b) dimensions of coupons (in mm) and (c) material test set-up.

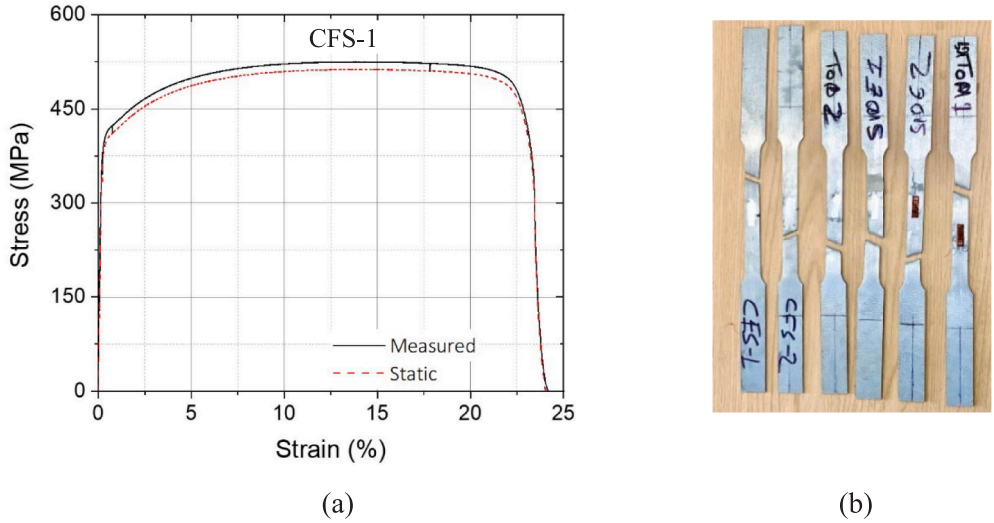

Fig. 6. (a) Stress–strain curve of CFS-1 coupon, sampled from the stud web of a tested wall specimen and (b) failed coupon specimens.

Table 4
Measured material properties of the CFS.

Coupons	$E_{,CFS}$ (GPa)	$f_{y,CFS}$ (MPa)	$f_{u,CFS}$ (MPa)	$\varepsilon_{u,CFS}$ (%)	$\varepsilon_{f,CFS}$ (%)
CFS-1	182	410	525	15	24
CFS-2	210	415	517	12	19
Top	214	480	520	8	13
Bottom	239	480	520	5	7
Side-1	226	490	529	7	13
Side-2	235	504	536	7	7
Average	218	463	525	9	14

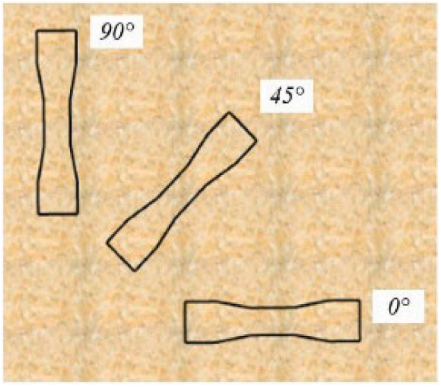

Fig. 7. Direction of coupons within the OSB board.

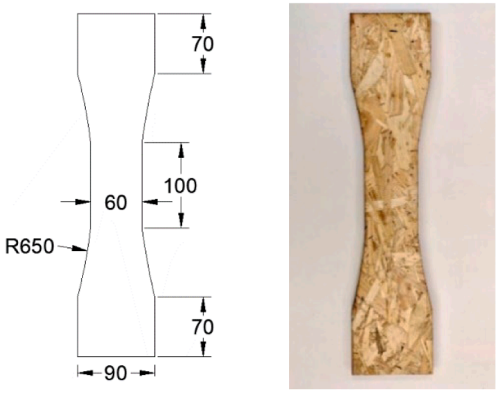

Fig. 8. OSB tensile coupon dimensions (in mm).

Table 5
Measured tensile properties of the OSB.

Specimens	$E_{t,OSB}$ (GPa)	$f_{t,OSB}$ (MPa)	$\varepsilon_{t,OSB}$
OSB-1_{ten} ($\alpha = 0°$)	2.1	13.1	0.009
OSB-2_{ten} ($\alpha = 45°$)	2.2	10.18	0.005
OSB-3_{ten} ($\alpha = 90°$)	2.1	11.30	0.008
Average	2.1	11.53	0.007

shear strengths obtained from the tests were compared with the available experimental data from literature and the theoretical predictions given by EN 1995 Part 1-1 [30].

A recent study conducted by Ringas et al. [31] investigated the screwed connections between CFS and CSB, using direct pull-out tests and monotonic and cyclic connector shear tests. The cyclic backbone curve showed good agreement with the monotonic curve, which implied that the effect of cyclic strength degradation was minor. In addition, a distinct pinching behaviour was observed in the hysteresis loop in both directions of loading due to gradual enlargement of the hole under bearing stresses.

Other relevant studies have assessed the out-of-plane bending behaviour of floor panels comprising CFS beams and wood-based boards through experimental and numerical investigations. Kyvelou et al. [32] conducted a series of four-point bending tests on such floor panels to study their composite action. It was found that the adhesive material used at the board–beam interface and the spacing of the fasteners significantly affect the flexural stiffness and moment capacity of the system. Based on the test results, a design method was proposed to predict the strength of the composite beams and the load–slip response of the fasteners connecting the boards to the CFS element. In a related study, Kyvelou et al. [33] numerically investigated composite action in the floor system, while considering the nonlinear interactions between all constituent components, and assessed the effects of critical parameters on the structural behaviour of the system, including the thickness and depth of the CFS sections, and the screw spacing. In another study, the effects of different types of fasteners (coach screws, self-drilling screws and bolts) on the load–slip behaviour of CFS–plywood

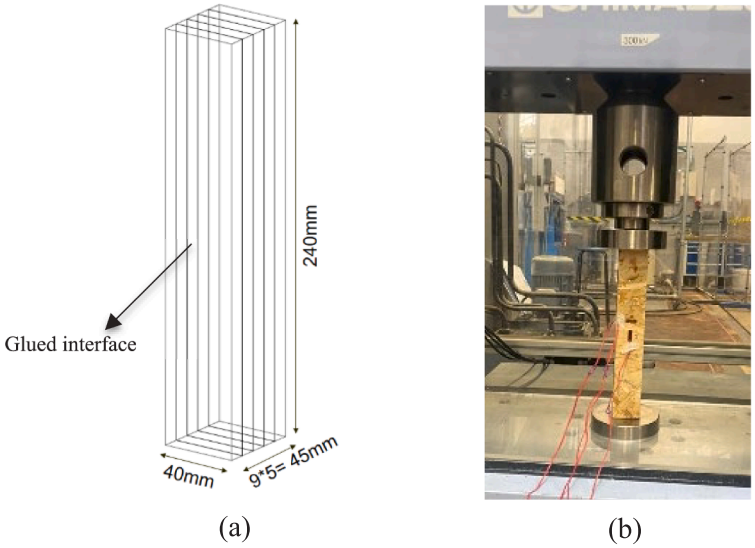

Fig. 9. OSB compressive coupons: (a) dimensions in mm and (b) test set-up.

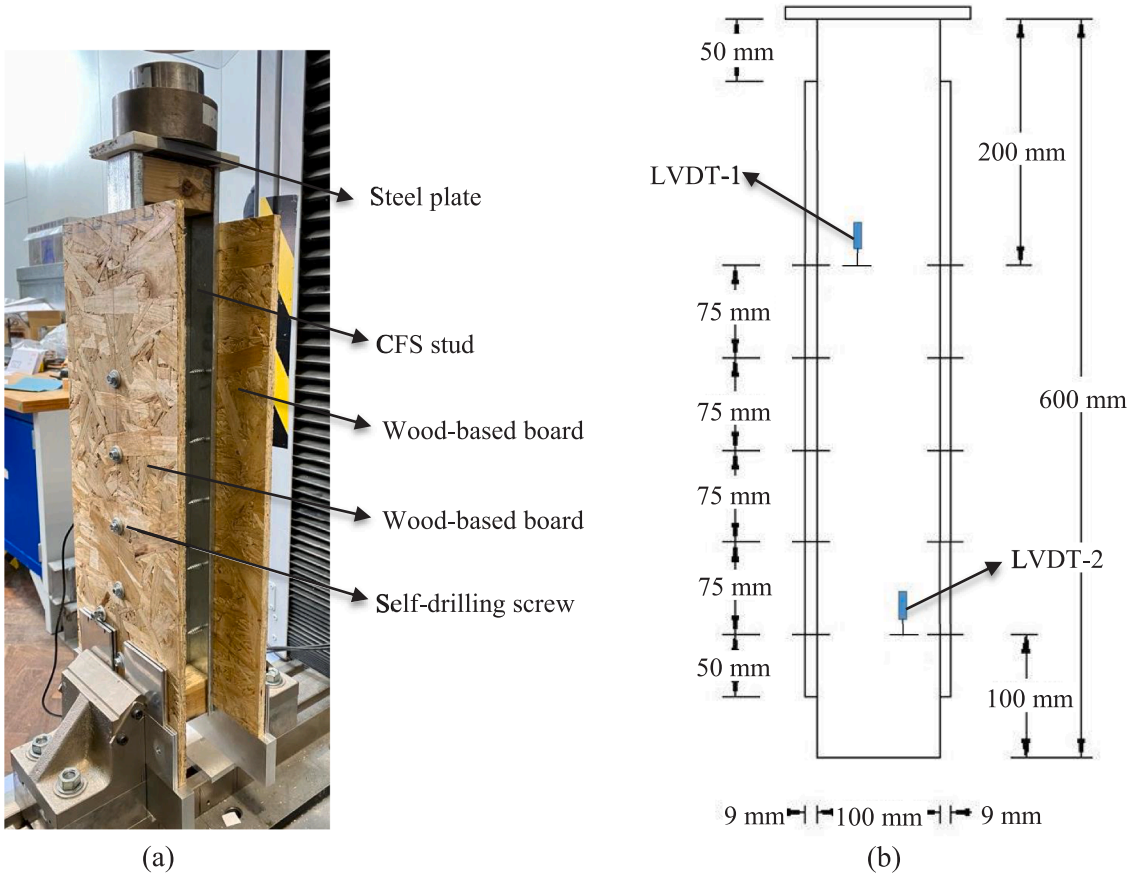

Fig. 10. (a) Push-out test set-up and (b) LVDT positions.

connections in floor systems were investigated by Karki et al. [34]. It was concluded that, while the bolted connections outperformed the self-drilling screws, the size of the bolts and nuts should be designed based on the strength of the plywood in order to prevent it from being crushed. The authors also proposed a simple new analytical expression to predict the load–slip response of the various connections.

In this paper the results are presented of a comprehensive experimental programme which aimed to investigate the flexural behaviour of OSB- and plywood-clad CFS stud wall panels under four-point bending. Bending in one direction was considered, particularly the direction which applies compression to the boards, so that the compressed flange of the studs benefits from the stabilizing effect of the boards (bending in the opposite direction is the subject of a currently ongoing study). A range of key design variables, including the screw spacing, the thickness of the CFS studs, the sheathing thickness and the board material were systematically varied in order to evaluate their effects. Both single-sided

Table 6
Measured compressive properties of the OSB.

Specimens	$E_{c,OSB}$ (GPa)	$f_{c,OSB}$ (MPa)	$\varepsilon_{c,OSB}$
OSB-1_{com} (α = 0°)	2.3	14.41	0.009
OSB-2_{com} (α = 45°)	2.4	13.6	0.007
OSB-3_{com} (α = 90°)	2.3	14.5	0.006
Average	2.3	14.17	0.007

Table 7
Ancillary connection test matrix.

Type of test	Specimen description	Test label	Width × Length (mm × mm)	Number of tests
Push-out tests	Key specimens Plywood (9 mm) OSB (18 mm) CFS (2 mm) No washer Screw spacing (300 mm)	$K1_{Push}$-$K2_{Push}$-$K3_{Push}$ $P9_{Push}$ $OSB18_{Push}$ $CFS2_{Push}$ UW_{Push} $S300_{Push}$	200 × 600	8
Pull-out tests	Key specimens	$K1_{Pull}$-$K2_{Pull}$-$K3_{Pull}$	300 × 300	3

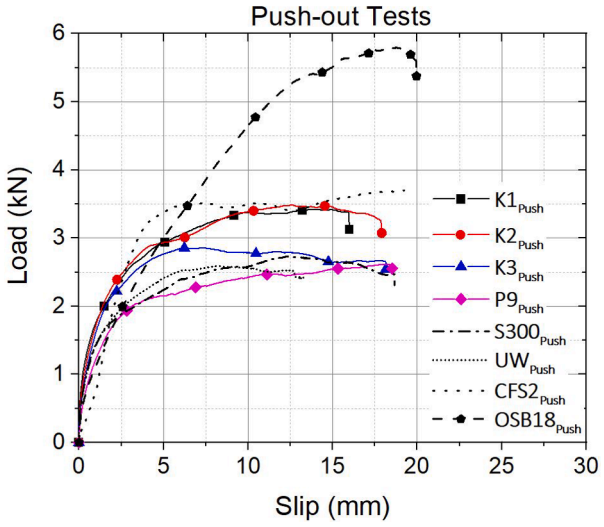

Fig. 11. Load–slip (*P-s*) responses in the push-out tests.

and double-sided sheathing were considered, the effect of longitudinal seams in the board was studied, and the influence of the presence/absence of noggins and top/bottom tracks was experimentally quantified.

2. Specimen geometry

A total of 15 full-height CFS stud wall specimens sheathed with wood-based materials were included in the experimental programme. Two identical specimens, labelled K1 and K2, were designated as the "key specimens" in the test matrix (Table 1), in order to set a benchmark for comparative purposes. The CFS track and stud elements comprised of plain (unlipped) channels and lipped channels, respectively, as illustrated in Fig. 1. The overall dimensions of the key specimens were 1220 × 2440 mm. They consisted of 1.2 mm thick CFS framing members (i.e. studs and tracks), connected to 9 mm thick single Oriented Strand Board (OSB) sheathing using 6.3 mm diameter self-drilling screws with a bonded washer (see Fig. 2) and a 75 mm screw spacing. The rest of specimens were designed with the aim of investigating a number of key design parameters, as described below:

- Four different spacings of 75, 100, 150 and 300 mm were considered for the connections between the CFS framing members and the wood-based boards around the panel perimeter and along the centre stud, as shown in Fig. 3(a).
- Different materials and thicknesses were considered for the boards: OSB with thicknesses of 9 mm and 18 mm, and structural plywood with a thickness of 9 mm (Fig. 3b). The OSB was graded OSB/3 according to EN 300 [35], while the plywood adhered to the requirements of EN 636 [36]. Both materials are therefore suited for use in humid conditions.
- Two different thicknesses were also considered for the CFS studs and framing elements: 1.2 and 2 mm (Fig. 3b).
- Unsheathed, single-sheathed and double-sheathed specimens were tested, as depicted in Fig. 3(c) and (d).
- Two different stud spacings of 305 and 610 mm were considered (Fig. 3e).
- One specimen contained a vertical seam in the boards along the centre stud in order to study its influence (Fig. 3g).
- The presence/absence of track sections and noggins was also considered, to experimentally quantify the restraint they provide (Fig. 3f).

A summary of the examined parameters is presented in Table 1.

A micrometre was used to accurately measure the dimensions of the wall components. The average out-to-out cross-sectional dimensions of the 1.2 mm thick and 2 mm thick CFS members are reported in Table 2. The thickness of the wood-based board (averaged over three different measuring locations at the top, middle and bottom of the board — see Fig. 4) are listed in Table 3.

3. Material tests

3.1. CFS members

Six flat tensile coupons were tested to determine the characteristics of the 1.2 mm thick CFS material. Four coupons were cut along the centrelines of the web and flanges of an intact channel stud, as depicted in Fig. 5(a). The remaining two coupons were sampled from the stud and track webs of actual wall specimens after the test. The nominal dimensions of all tensile coupons were kept the same, with a nominal gauge width of 12.5 mm, as recommended by the EN ISO 6892-1 specifications [37] (Fig. 5b). Each flat coupon was instrumented with a 50 mm extensometer and two 10 mm strain gauges (one on each side) to accurately record longitudinal strains in the early stages of testing (Fig. 5c). The zinc coating was removed from the coupons before attaching the strain gauges.

The tensile tests were conducted according to EN ISO 6892-1 [37] in a displacement-controlled manner using a 300 kN Shimadzu testing machine (Fig. 5c). The displacement rate was set at 0.50 mm/min. To eliminate the effect of the strain rate on the mechanical properties of the CFS [38], the tensile test was paused two times: once the yield stress was reached, and once near the ultimate strength. The test results of all six CFS coupons are presented in Table 4, which lists Young's modulus (E_{CFS}), the yield stress ($f_{y,CFS}$), the ultimate strength ($f_{u,CFS}$), the strain corresponding to the ultimate strength ($\varepsilon_{u,CFS}$), and the strain at fracture ($\varepsilon_{f,CFS}$). As an example, the measured stress–strain curve of one of the coupons taken from the stud web of a tested wall specimen is reproduced in Fig. 6, which also shows all coupons after failure. The lower-bound 'static' stress–strain curve is also shown in Fig. 6(a), which was

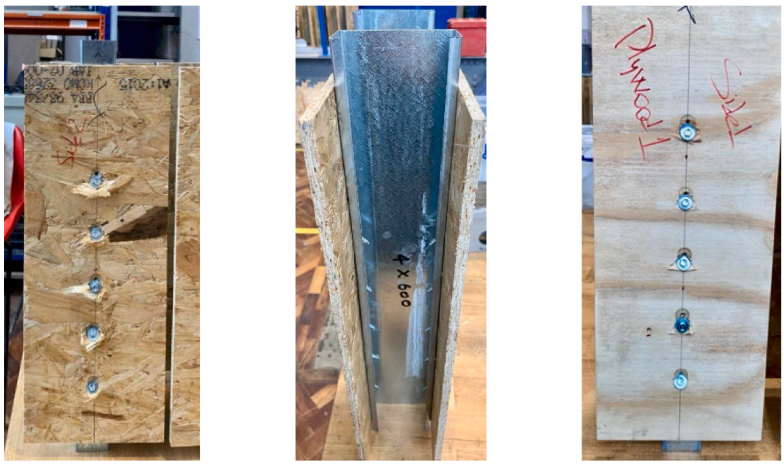

(a) $K1_{Push}$ (b) $OSB18_{Push}$ (c) $P9_{Push}$

Fig. 12. Typical failure mode captured from the push-out tests.

Table 8
Push-out test results: main performance parameters.

Specimen batch	P_u (kN)	S_u (mm)	R_i (kN/mm)
$K1_{Push}$	3.42	13.70	2.39
$K2_{Push}$	3.48	12.67	2.16
$K3_{Push}$	2.85	7.25	2.20
$P9_{Push}$	2.61	18.04	1.95
$OSB18_{Push}$	5.79	18.77	2.36
$CFS2_{Push}$	3.69	19.18	2.18
UW_{Push}	2.59	8.26	2.22
$S300_{Push}$	2.73	12.30	2.05

obtained by reducing the stress values to levels consistent with those observed during the loading pauses.

3.2. OSB boards

Since the material properties of OSB are different in tension and compression, separate experiments were conducted to determine its tensile and compressive properties. The tests were conducted according to EN 789 [39]. For each loading condition, three coupons were cut: one in each of the following directions relative to the longitudinal direction of the board: $\alpha = 0°$, 45°, and 90°, as shown in Fig. 7.

3.2.1. Tensile coupon tests

The dimensions of the 9 mm thick tensile coupons were determined in accordance with EN 789 [39], and are presented in Fig. 8. The load was applied using a 300 kN Shimadzu universal testing machine employed in a displacement-controlled manner with a constant axial displacement rate of 0.25 mm/min, also consistent with EN 789 [39]. Each tensile coupon was instrumented with four 10 mm strain gauges mounted at the centre of the specimen. Table 5 lists the measured modulus of elasticity ($E_{t,OSB}$), the ultimate tensile strength ($f_{t,osb}$) and the corresponding ultimate strain ($\varepsilon_{t,OSB}$) for all tensile coupons. No statistically significant anisotropy could be detected.

3.2.2. Compression tests

Compressive coupons were extracted from the 9 mm thick OSB in

Table 9
Pull-out test results: main performance parameters.

Specimen batch	P_u (kN)	s_u (mm)	R_i (kN/mm)
K1	1.98	10.74	0.24
K1	1.73	9.60	0.21
K3	1.86	8.45	0.26

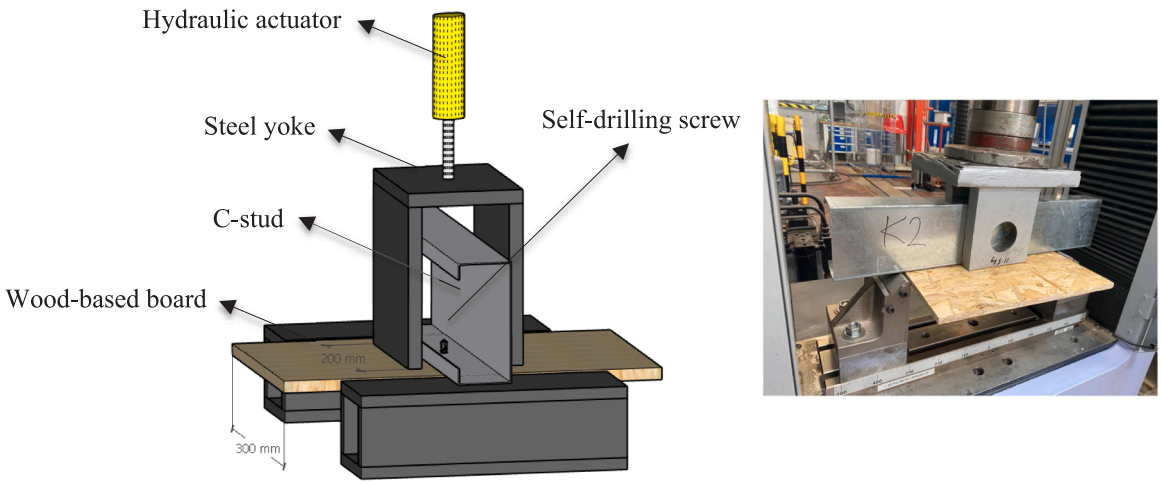

Fig. 13. Test set-up of the pull-out tests.

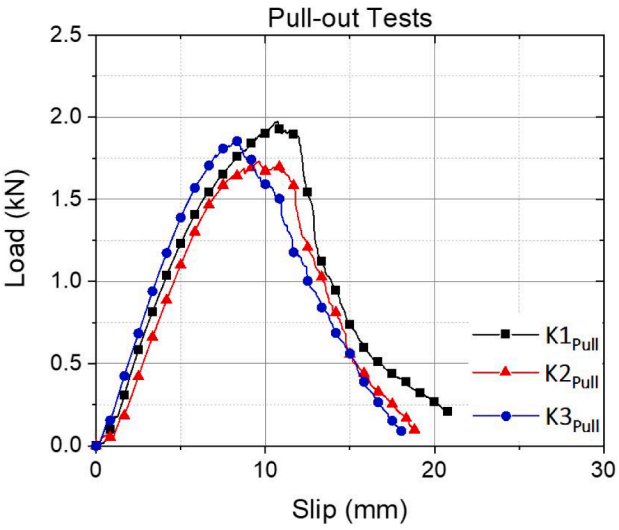

Fig. 14. Load–slip (P-s) response of the pull-out specimens.

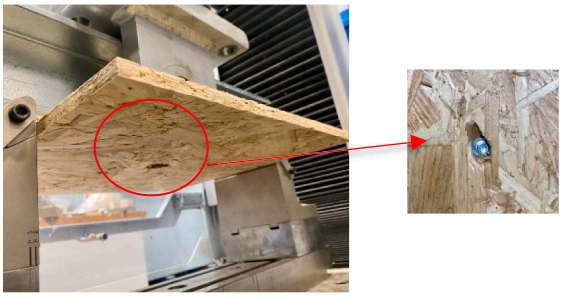

Fig. 15. Typical failure mode captured from the pull-out tests.

order to obtain its compressive mechanical properties in the in-plane direction. Each compressive coupon was assembled from five rectangular pieces of board material with dimensions of 50 mm × 240 mm (see Fig. 9), in line with BS EN 789 [39]. The five pieces were glued together using outdoor epoxy adhesive, as shown in Fig. 9. Coupons were produced in three different directions (α = 0°, 45°, and 90°). The compressive load was applied using a 300 kN Shimadzu universal testing machine in a displacement-controlled manner, and a constant

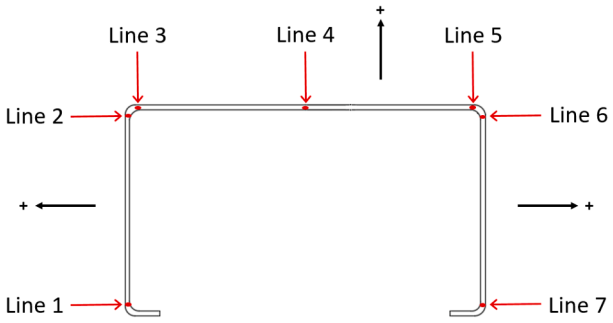

Fig. 17. Locations of imperfection measurement lines on lipped channel.

Table 10
Maximum amplitudes of local and distortional imperfections (in mm).

Specimen	Local	Distortional-1	Distortional-2
C1	0.35	0.07	0.17
C2	0.58	0.14	0.22
C3	0.34	0.11	0.24
C4	0.49	0.17	0.36
C5	0.81	0.26	0.13
C6	0.36	0.22	0.21
Average	0.49	0.16	0.22

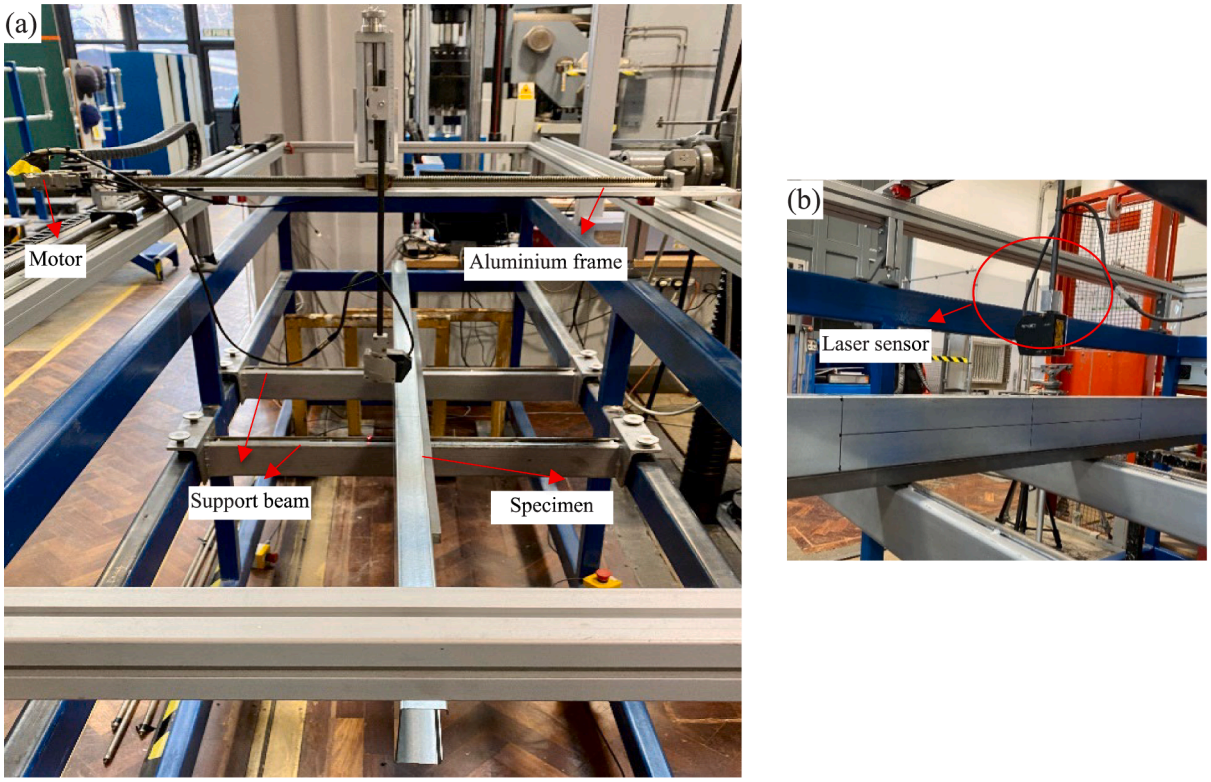

Fig. 16. (a) Test set-up, (b) laser sensor.

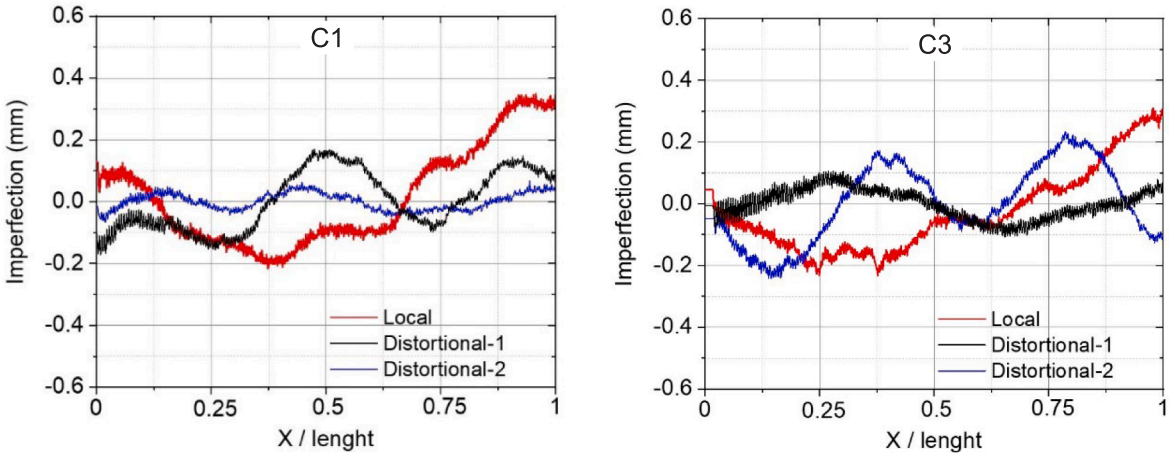

Fig. 18. Typical imperfections recorded along the length of CFS lipped channel members.

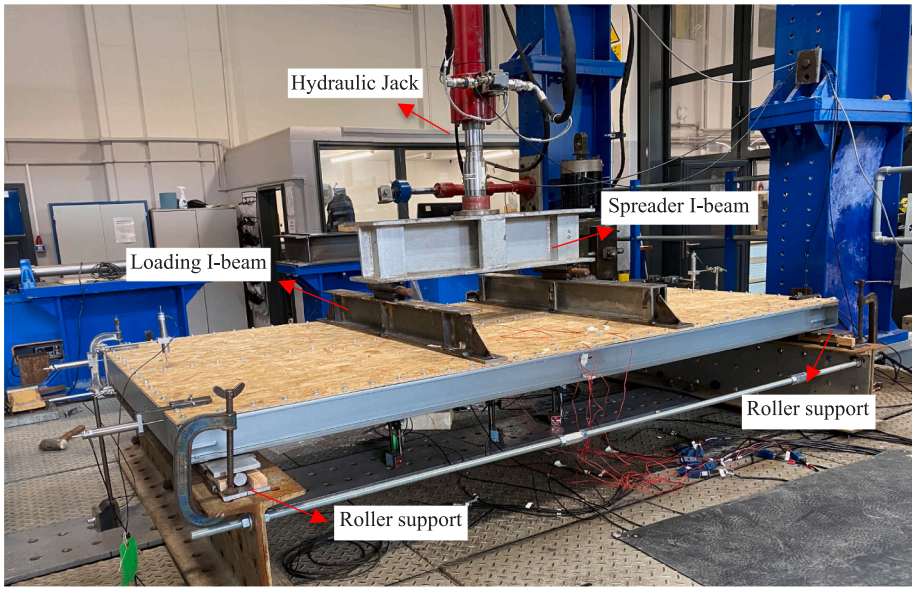

Fig. 19. Test set-up.

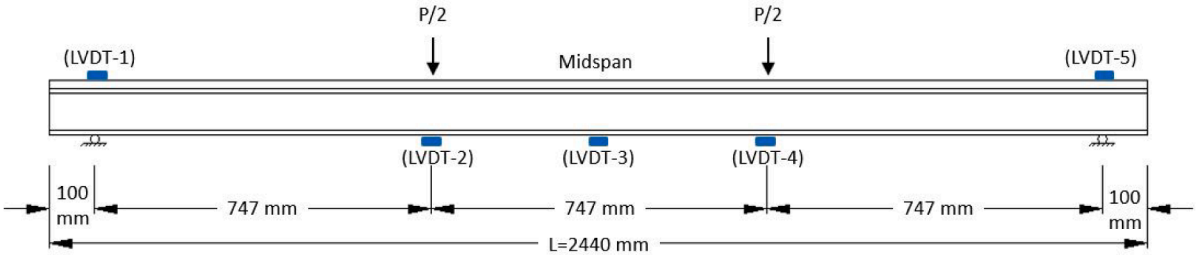

Fig. 20. Schematic 2D view of the test set-up and the locations of the LVDTs.

displacement rate of 0.50 mm/min was applied until failure. Each specimen was instrumented with four 10 mm strain gauges, as depicted in Fig. 9.

The measured compressive properties of the OSB material are presented in Table 6, where $E_{c,OSB}$ represents the modulus of elasticity, and $f_{c,OSB}$ and $\varepsilon_{c,OSB}$ are the ultimate compressive stress and the associated strain, respectively. Properties were found to be nominally isotropic.

4. Ancillary connection tests

It has frequently been demonstrated in the literature that the capacity and failure mode of sheathed CFS stud wall systems under various types of loading are directly dependent on the behaviour of the fasteners [4,9,15–18]. To obtain an insight into the behaviour of the CFS-to-sheathing connections, a series of push-out and pull-out tests were conducted on a total of 11 small-scale subassemblies. The test matrix is presented in Table 7. Each connection test was representative of a

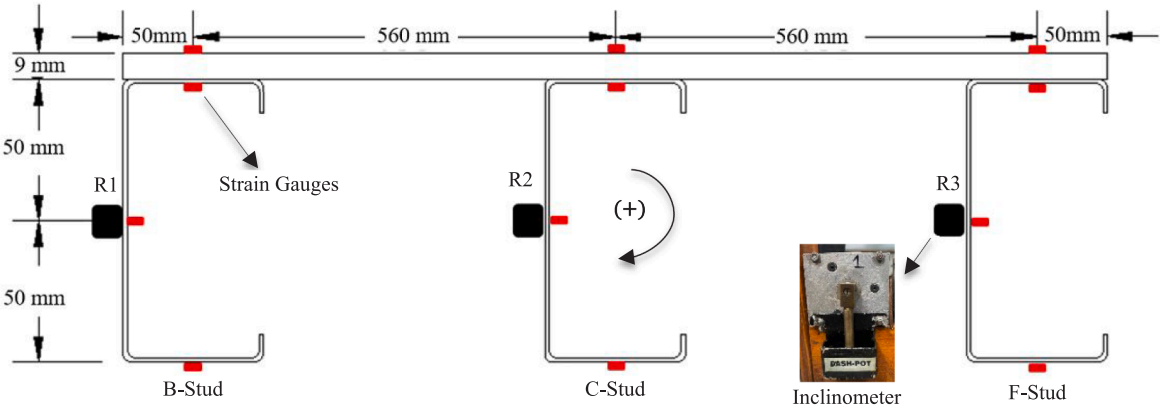

Fig. 21. Positions of inclinometers and strain gauges at panel midspan.

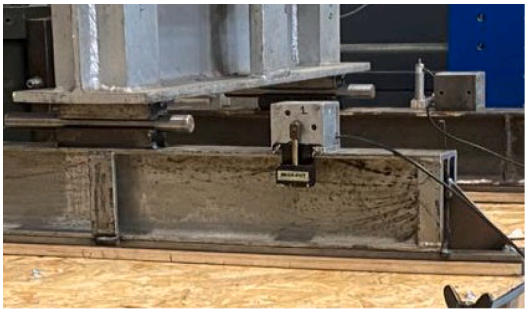

Fig. 22. Position of inclinometers on the loading beams.

particular full-scale configuration listed in Table 1. For instance, $K1_{Push}$ represents a push-out test on the key specimen connections (K1 and K2), where five self-drilling screws with a spacing of 75 mm were used to connect a 9 mm thick OSB board to the flanges of a 1.2 mm CFS stud. In both the pull-out and the push-out tests, the load was applied using a 300 kN Shimadzu testing machine employed in a displacement-controlled manner with constant displacement rates of 1.0 and 0.5 mm/min, respectively. The data acquisition system was controlled by National Instruments LabView software and produced data with a sampling rate of 1 Hz.

4.1. Push-out tests

A schematic view of the push-out test arrangement is shown Fig. 10 (a). Lipped channel CFS stud segments with a length of 500 mm and

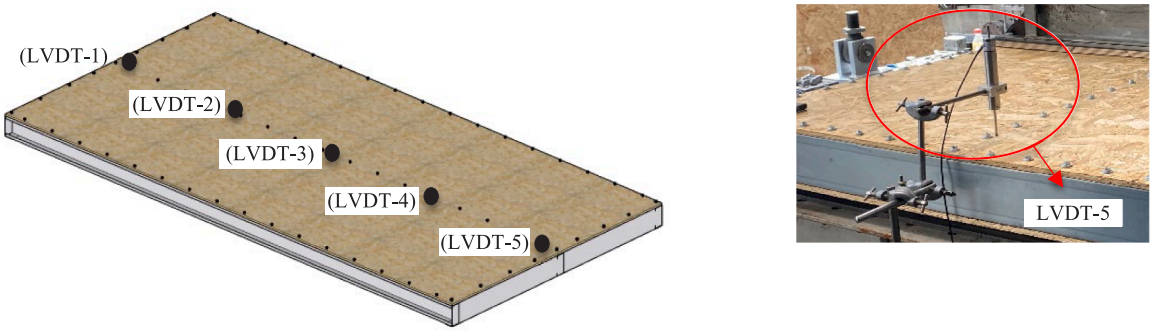

Fig. 23. Positions of five LVDTs along centreline of panel.

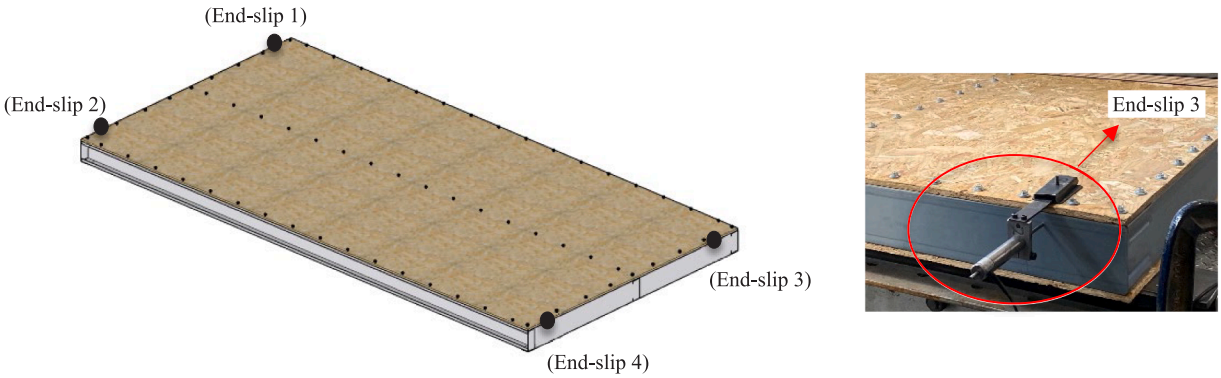

Fig. 24. Positions of four LVDTs for end slip measurements.

Table 11
Main structural performance parameters and observed failure modes of each test specimen.

Specimen	Initial stiffness (kN/mm)	Peak load (kN)	Deflection at peak load (mm)	Ultimate displacement (mm)	Observed failure mode
K1	1.1	29.2	33.3	41.6	Distortional buckling/ Board crushing
K2	1.1	30.6	36.9	43.6	Distortional buckling/ Board crushing
S100	1.1	29.9	38.4	54.6	Distortional buckling/ Board crushing
S150	1.1	25.6	30.5	56.7	Distortional buckling/ Board crushing
S300	1.0	22.8	30.8	72.4	Distortional buckling/ Board crushing/ Screw tilting and bearing failure at specimen ends
P9	1.0	30.7	44.9	54.1	Lateral-torsional buckling/ Longitudinal plywood fracture
OSB18	1.2	38.9	68.3	83.4	Lateral-distortional Buckling
CFS2	1.6	54.5	48.6	59.6	Lateral-(dis) tortional buckling/ Local buckling/ longitudinal board fracture/Board crushing
UB	0.5	8.0	50.5	67.9	Lateral-torsional buckling
DB1	1.6	33.7	23.4	37.8	Local-distortional buckling/ Board crushing
DB2	1.6	35.4	26.4	38.5	Local-distortional buckling/ Board crushing
DR	1.0	29.3	35.0	37.5	Distortional buckling/ Board crushing/ Screw bearing failure
S	1.1	31.3	38.3	59.9	Distortional buckling/ Board crushing
N	1.3	31.1	42.0	46.7	Distortional buckling/ Board crushing and buckling
NT	1.1	25.8	28.9	30.0	Lateral-torsional buckling/ Board failure (folding) at specimen ends

cross-sectional dimensions of 100 × 50 × 10 (in mm) were used. Both flanges of the lipped channel stud were connected to 200 × 425 mm^2 wood-based boards using 6.3 mm diameter self-drilling screws with bonded washers (see Fig. 2). Compression was applied to the CFS channel, in order to subject the connections to shear and record the load–slip behaviour of the screws. Various design parameters were considered: (i) OSB vs. plywood boards, (ii) various OSB and CFS thicknesses, (iii) various screw spacings and (iv) the effect of a washer. Two linear variable differential transformers (LVDTs) were employed to measure slip at the locations of the first and last connectors (Fig. 10b). These LVDTs were supported from the boards, with their tips pushing off against 50 mm

The load–slip (P-s) responses of all specimens are presented in Fig. 11, where P is the load per screw and s is the slip calculated by averaging the values obtained from the two LVDTs. In addition, a summary of the ultimate load per connector (P_u), the slip at the ultimate load (s_u) and the initial stiffness of each connection (R_i) is reported in Table 8. All specimens exhibited a similar failure mechanism, where tilting of the screws as well as bearing failure against the wood-based boards was observed (Fig. 12). It can be seen from Table 8 that increasing the OSB thickness from 9 mm to 18 mm resulted in an increase of 80% in connection strength. Increasing the CFS thickness from 1.2 mm to 2 mm, on the other hand, resulted in only a minor increase of 14% in the connection strength. When comparing the responses of plywood and OSB connections for the same connection configuration (i.e. thickness and screw spacing), it can also be concluded that using plywood provided slightly lower stiffness and strength (with reductions of 19% and 24%, respectively). The results also demonstrated that the presence of washers slightly improved the connection strength (by 25% on average). While increasing the screw spacing from 75 mm to 300 mm appeared to decrease both the strength and stiffness of the connections by 14% and 9%, respectively, these variations, observed in a single test, might not be statistically meaningful (as the COVs of the key specimens were 11% and 28% for strength and stiffness, respectively).

4.2. Pull-out tests

The load–slip response of the connections under tensile loading in the out-of-plane direction was determined through a series of monotonic pull-out tests. Each specimen consisted of a 300 × 300 mm^2 OSB board, connected with a single screw to the flange of a 500 mm long CFS stud segment. Three specimens with the characteristics of the connections employed in the full-scale key specimens were tested. A schematic view of the pull-out test arrangement is shown in Fig. 13. A U-shaped steel yoke was used to directly transfer the applied load to the board and subject the screw to tensile loading.

The load–slip *(P-s)* responses of all specimens are depicted in Fig. 14, where P is the load per screw and s is the slip measured by the actuator's datalogger. A summary of the main performance parameters is also provided in Table 9, where P_u is the ultimate pull-out load per connector, s_u is the out-of-plane displacement at the ultimate load and R_i is the initial connection stiffness.

As expected, all pull-out specimens showed a similar load–slip response over the whole range of loading (Fig. 14). Pull-through of the screw was observed to be the dominant failure mode in all three specimens, as shown in Fig. 15. In general, less ductile behaviour was observed when the screws were loaded in tension, compared to shear.

5. Initial imperfection measurements

Imperfections can have a significant impact on structural stability, especially in thin-walled structural members when coupled instabilities are involved [40–43]. Therefore, the geometric imperfections of six test specimens were measured using a specially designed imperfection

Table 12
Longitudinal end slip readings at the four corners of each specimen (in mm).

Specimens	At peak load				At ultimate deflection			
	End-slip 1	End-slip 2	End-slip 3	End-slip 4	End-slip 1	End-slip 2	End-slip 3	End-slip 4
K1	0.36	0.22	0.15	0.12	0.63	0.43	0.16	0.14
K2	0.22	0.43	0.28	0.39	0.34	0.53	0.34	0.45
S100	0.31	0.36	0.33	0.42	0.53	0.45	0.49	0.53
S150	0.37	0.57	0.53	0.71	2.11	1.07	1.10	2.11
S300	0.95	1.38	0.85	1.50	1.73	7.13	1.90	9.18
P9	0.78	0.50	0.73	0.25	1.14	0.55	0.97	0.29
OSB18	0.97	1.33	0.75	1.26	1.38	1.59	1.12	1.53
CFS2	0.53	0.40	0.24	0.40	0.79	0.41	0.34	0.42
DB1	0.04	0.29	0.09	0.33	0.17	0.37	0.21	0.36
DB2	0.11	0.25	0.14	0.32	0.22	0.28	0.27	0.33
	0.29	0.50	0.25	0.54	0.34	0.58	0.33	0.68
DR								
S	0.32	0.60	0.35	0.56	0.57	0.69	0.41	0.75
N	0.42	0.65	0.50	0.65	0.43	0.69	0.51	0.70

Table 13
Rotations of studs about their longitudinal axis and rotations of loading beam.

Specimens	At peak load				At ultimate displacement			
	B-Stud R1 (°)	C-Stud R2 (°)	F-Stud R3 (°)	Loading beam (°)	B-Stud R1 (°)	C-Stud R2 (°)	F-Stud R3 (°)	Loading beam (°)
K1	7.89	6.98	12.00	–	8.17	8.10	12.10	–
K2	8.34	8.24	12.00	–	8.89	10.48	11.95	–
S100	8.73	9.29	14.05	0.14	9.87	9.40	14.07	1.60
S150	6.29	8.26	10.59	0.34	7.33	8.48	13.42	1.14
S300	7.55	10.26	11.19	0.40	9.09	10.47	13.00	−2.49
P9	11.94	11.19	24.6	0.50	12.43	11.68	37.68	1.89
OSB18	9.20	10.55	17.27	0.26	14.36	10.69	49.11	2.35
	14.09	–	12.05	–	14.25	–	12.35	–
CFS2								
UB	20.76	–	32.37	1.07	32.67	–	57.21	3.13
DB1	0.15	–	–	0.14	7.02	–	–	1.23
DB2	−0.43	–	–	0.13	4.39	–	–	1.13
	6.68	8.5	10.65	0.38	9.92	10.73	12.00	1.25
DR								
S	8.18	9.24	15.14	0.42	10.07	12.08	24.10	2.53
N	3.17	1.18	0.48	0.27	6.31	3.22	1.64	−1.00
	6.12	4.42	3.36	0.77	3.41	5.62	6.28	1.21
NT								

Some data was not recorded due the inclinometers falling off the specimen; in the case of the specimens with boards on both sides, only the web of the B-stud was accessible.

measuring rig, shown in Fig. 16. The rig consisted of a traverse system with two electric motors with the ability to move a Keyence LK-G82 laser sensor in two orthogonal directions. During the measuring process, the laser sensor was moved longitudinally along the specimens at a speed of 5 mm/s, while readings were taken at a sampling rate of 5 Hz, resulting in one reading every millimetre. The accuracy of the frame is of the order of ±0.07 mm, which is the straightness tolerance of the longitudinal guidance bars [44].

The imperfections were measured along seven longitudinal lines on the CFS members, as shown in Fig. 17, including three lines on the web and two lines on each flange. The imperfection data was further used to determine representative magnitudes of the local and distortional imperfections. The local imperfection was calculated by subtracting the average reading along lines 3 and 5 from the reading taken along line 4. To calculate the distortional imperfection the readings along line 1 (or 7) were first subtracted from those along line 2 (or 6). The results were then adjusted so that the average distortional imperfection along the flange length was zero [44]:

$$\text{Distortional-1}: \delta'_{flange,1}(x) = (\text{Line}\quad 1 - \text{Line}\quad 2) \tag{1}$$

$$\delta_{flange,1}(x) = \delta'_{flange,1}(x) - \text{Average}\left(\delta'_{flange,1}(x)\right)$$

$$\text{Distortional-2}: \delta'_{flange,2}(x) = (\text{Line}\quad 7 - \text{Line}\quad 6) \tag{2}$$

$$\delta_{flange,2}(x) = \delta'_{flange,2}(x) - \text{Average}\left(\delta'_{flange,2}(x)\right)$$

$$\text{Local}: \delta_{web}(x) = \text{Line}\quad 4 - \left(\frac{\text{Line}\quad 3 - \text{Line}\quad 5}{2}\right) \tag{3}$$

The maximum recorded amplitudes of the local and distortional imperfections are listed in Table 10 for the six measured channels. The maximum out-of-plane imperfections encountered in the webs of the channels were of the order of 0.81 mm, while the flanges of the channels exhibited distortional imperfections of up to 0.36 mm. Fig. 18 presents two examples of imperfection profiles recorded along the length of the members.

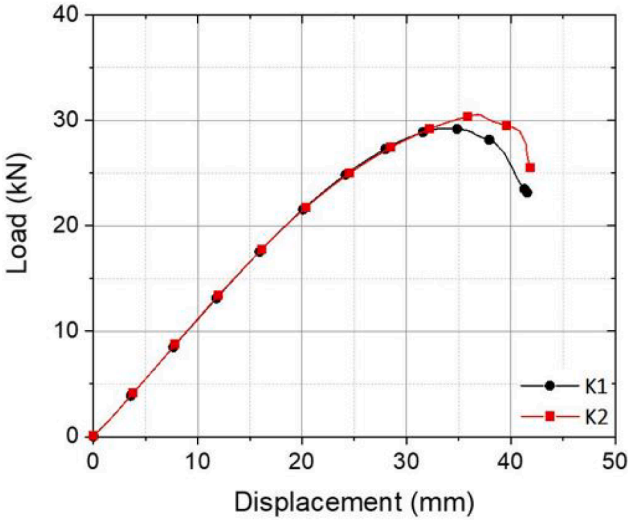

Fig. 25. Load–displacement response of key specimens.

6. Test set-up and instrumentation

All wall panels were tested in four-point bending. The loading was applied directly to the boards in a way which simulated wind pressure acting towards the inside of the building. The test set-up is illustrated in Fig. 19. An I-shaped spreader beam was used to transfer the load from the 150 kN hydraulic jack to two I-shaped loading beams running across the width of the board. The distance between the loading beams was equal to 747 mm, or one-third of the total span. The studs were positioned with a 100 mm overhang at each support point (Fig. 20). Wooden blocking was provided within the stud cross-sections under the loading beams and over the supports, to prevent localized failure involving web crippling, and to ensure failure within the constant moment zone.

A data acquisition system, which was controlled by the National Instruments LabView software, accumulated data at a sampling rate of 1 Hz. A constant displacement rate of 2 mm/min was applied.

Each panel comprised three studs. In what follows, the middle stud is denoted by the character "C", while the two boundary studs are indicated by "B" and "F". Strain gauges were attached to the boards and the CFS elements at mid-span, as shown in Fig. 21. To monitor the cross-sectional rotation of each CFS stud, an inclinometer was installed on each web at mid-span (Fig. 21). Additional inclinometers were also mounted on each transverse loading beam in order to measure the rotations of the stud wall system about its longitudinal axis, as illustrated in Fig. 22. A total of nine LVDTs were installed: three LVDTs were placed on the bottom flange of the middle stud, supported from the floor, at mid-span and under the loading points, and two LVDTs were positioned on the boards over the supports to monitor support settlement (see Figs. 20 and 23). Additionally, the end slip between the studs and the boards was measured using four LVDTs, placed horizontally at the four corners of the specimen (and labelled 'End-slip 1', 'End-slip 2', 'End-slip 3' and 'End-slip 4'), as shown in Fig. 24.

7. Test results

The main structural performance parameters obtained from the four-point bending tests are summarized in Table 11, including the initial stiffness of the system, the peak load and its corresponding deflection, the ultimate deflection, and the observed failure modes. The initial stiffness was defined as the initial slope of the load–deflection (P-δ) curve and calculated based on the points at 10% and 40% of the ultimate load. The ultimate deflection was defined as the deflection corresponding to a 20% post-peak drop in load. In addition, Tables 12 and 13 present a series of complementary results, consisting of the LVDT end slip readings and the stud rotations, which are reported at two different loading stages: (i) at the peak load and (ii) at the ultimate displacement. The test results are further discussed in the following sub-sections which elaborate on the effects of various test parameters.

7.1. Key specimens

Fig. 25 plots the applied load versus the vertical deflection at the centre of the panel (LVDT-3) for the key specimens (K1 and K2). Very consistent behaviour was obtained for these two nominally identical specimens: the maximum load carried by the K1 and K2 specimens reached 29.2 kN and 30.6 kN, respectively, and the deflections at the peak load were measured to be 33 and 37 mm. Both specimens failed within the constant moment span by a combination of distortional buckling in the steel channel and localized crushing of the OSB in the same cross-section, as shown in Fig. 26.

The strain gauge measurements are plotted versus the applied load in Fig. 27 for key specimen K1, with tensile strains considered positive. The readings are very consistent across the B-, C- and F-studs. By comparing the readings on the channel top flange with those on the OSB, it is also concluded that very good composite action was achieved in the initial stages of loading. Comparatively larger strains developed in the top flange of the channel once buckling initiated.

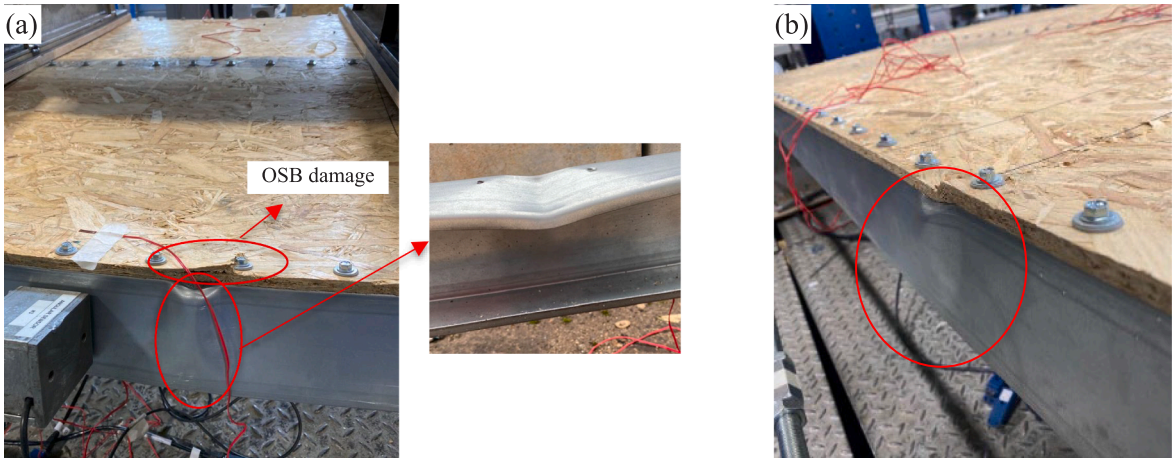

Fig. 26. Failure modes of: (a) K1 and (b) K2 specimens.

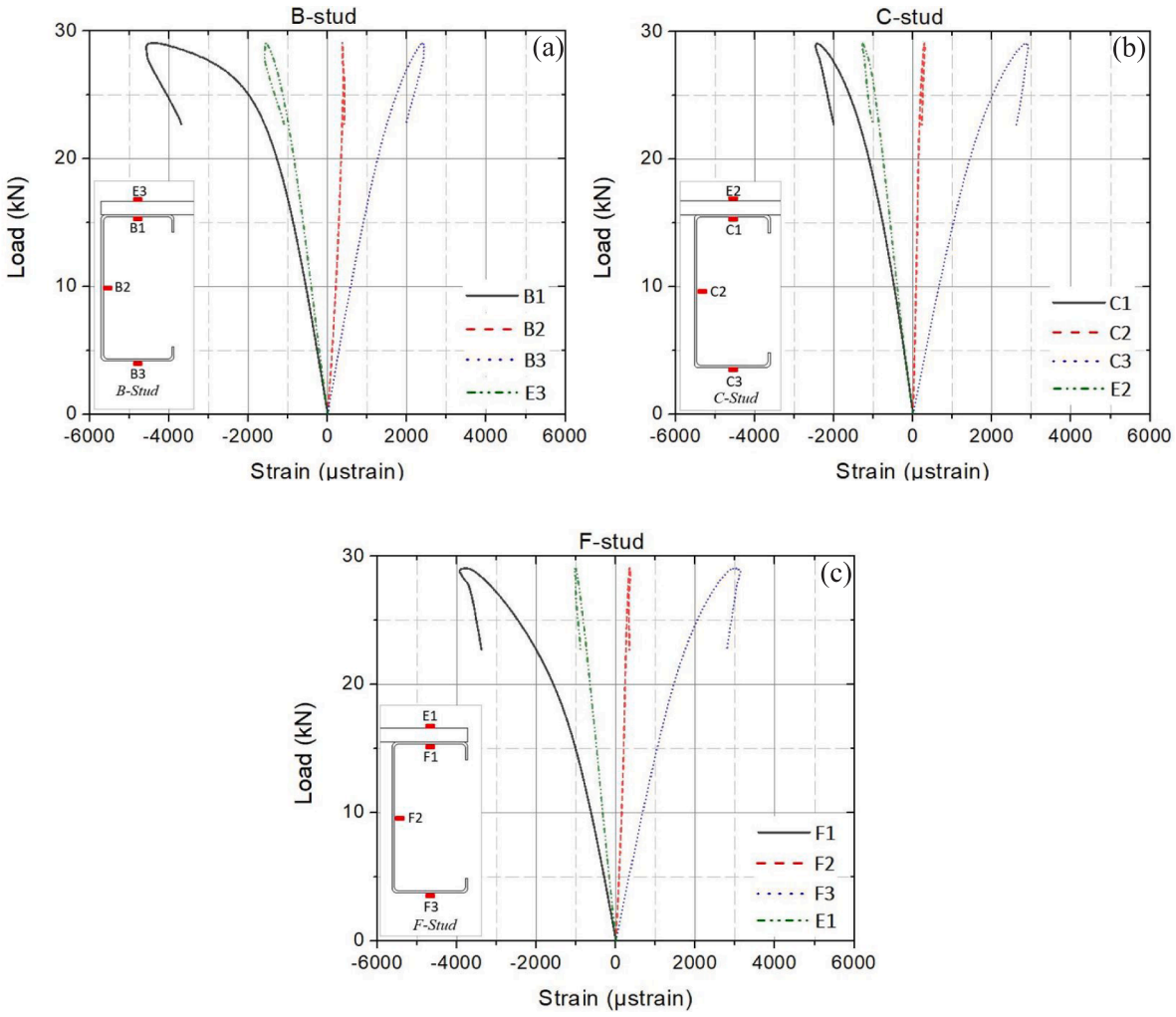

Fig. 27. Load–strain curves in studs and OSB for K1 specimen at various locations: (a) B-stud, (b) C-stud and (c) F-stud.

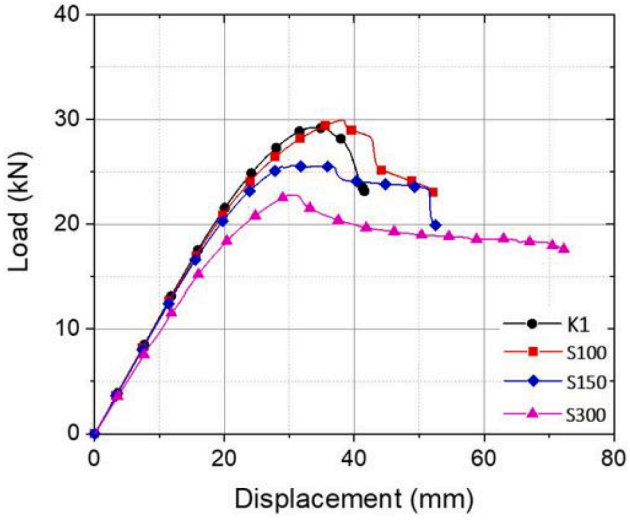

Fig. 28. Load–displacement responses of stud walls with increasing screw spacing.

The twist of the panel about its longitudinal axis remained limited until buckling originated in the channels. However, near failure larger twist rotations occurred towards the B-stud, which displayed the largest vertical deflections and the most prominent failure.

7.2. *Influence of screw spacing*

Fig. 28 compares the response of key specimen K1 (featuring a 75 mm screw spacing) to those of similar specimens with increased screw spacings of 100 mm, 150 mm and 300 mm. While near identical capacities were obtained for the 75 mm and 100 mm screw spacings, increasing the spacing to 150 mm and 300 mm led to significant reductions in capacity of 14% and 24%, respectively. Similarly, comparable values of the overall bending stiffness were obtained for 75 mm to 150 mm spacings, but a reduction by 9% was observed for the 300 mm screw spacing (Table 11). On the other hand, the specimen with 300 mm screw spacing displayed a more ductile failure behaviour, sustaining a more gradual and less steep post-peak descent (Fig. 28).

The observed failure mechanism was the same across the various screw spacings considered, and consisted of distortional buckling of the channel studs alongside crushing of the OSB, as pictured in Fig. 29. In the case of 300 mm screw spacing, significant bearing damage was also observed in the OSB around the screws in the corners of the panel (Fig. 29d). In relation to this, Fig. 30 compares the end slip readings for specimens K1 and S300. It is seen that the slip values in the S300

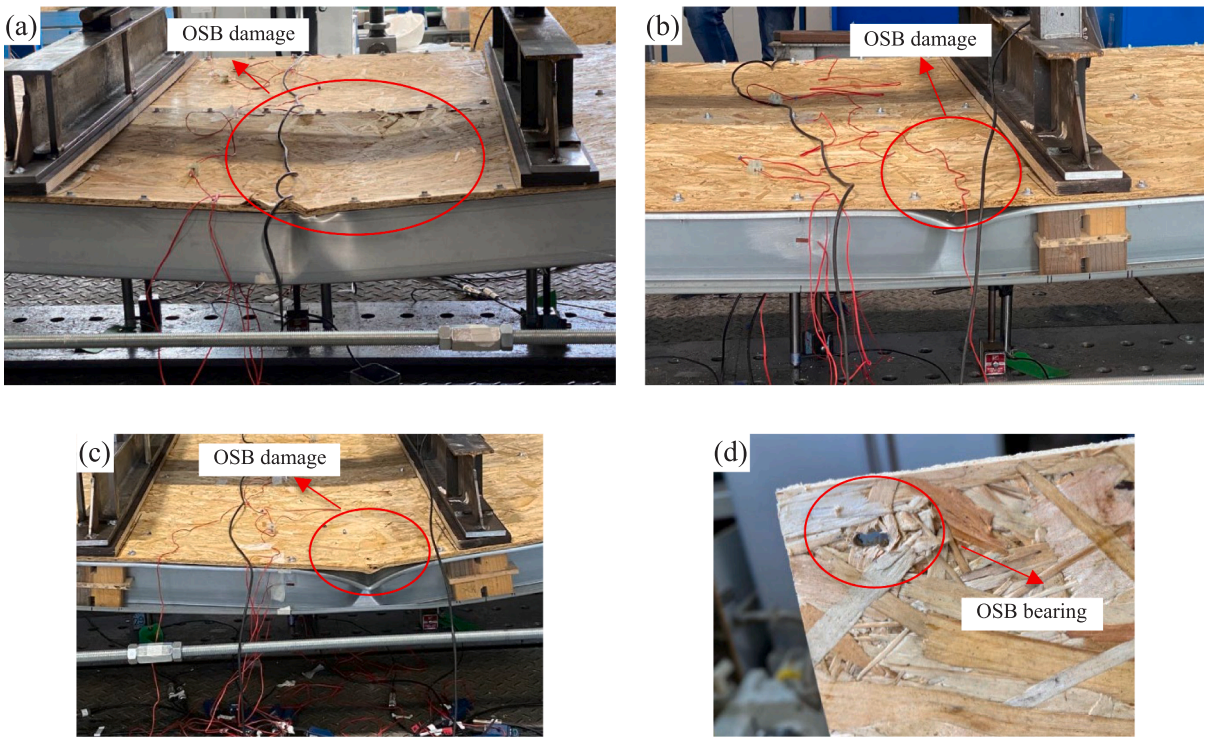

Fig. 29. Failure modes of (a) S100, (b) S150, (c) and (d) S300 specimens.

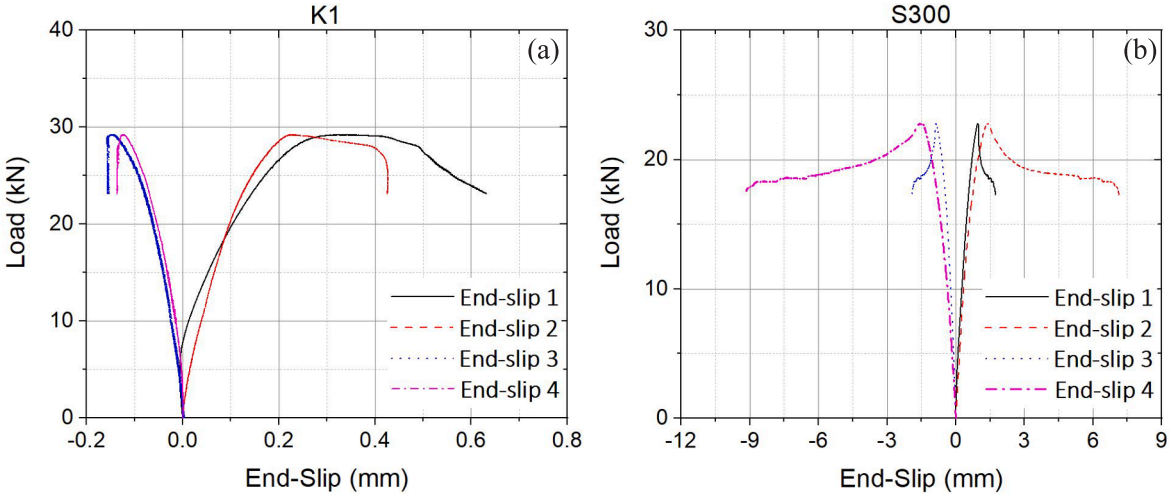

Fig. 30. End-slip measurement for: (a) K1 and (b) S300 specimens.

specimen are an order of magnitude larger than in the key specimen.

The strain gauge readings for specimen S300 are presented in Fig. 31. Complete results for all test specimens can be found in [45] and further confirm the observed trends. It is clear that the strains in the OSB are significantly lagging behind those in the channel top flange and that, as a result of pronounced slip between the channels and the board, full composite action is no longer achieved.

From the above, it can be concluded that the reasons for the reduction in bending capacity with increasing screw spacing can be found in an increased slip, a loss in the degree of composite action, and a reduction in the distortional buckling stress of the channel as a result of a longer imposed buckling half-wavelength (i.e. one closer to the natural half-wavelength — see Fig. 28).

7.3. Influence of the board material and thickness

Fig. 32 and Table 11 show that doubling the thickness of the OSB from 9 mm to 18 mm increased the bending capacity of the panel by 33% (from 29.2 kN to 38.9 kN). Importantly, the increase in thickness also altered the observed failure mode. Crushing of the OSB no longer occurred. Instead, the channel studs deformed in a combination of lateral distortion and torsion about the connection point with the OSB, the latter made possible by localized plastic deformations around the screws (Fig. 33a,b). From the strain gauge readings, presented in Fig. 34, it is also seen that full composite action was achieved in the initial loading range.

In specimen P9 the OSB was replaced by 9 mm thick structural grade plywood boards. Fig. 32 indicates that the ultimate bending capacity and initial stiffness of P9 were roughly comparable to those of the key

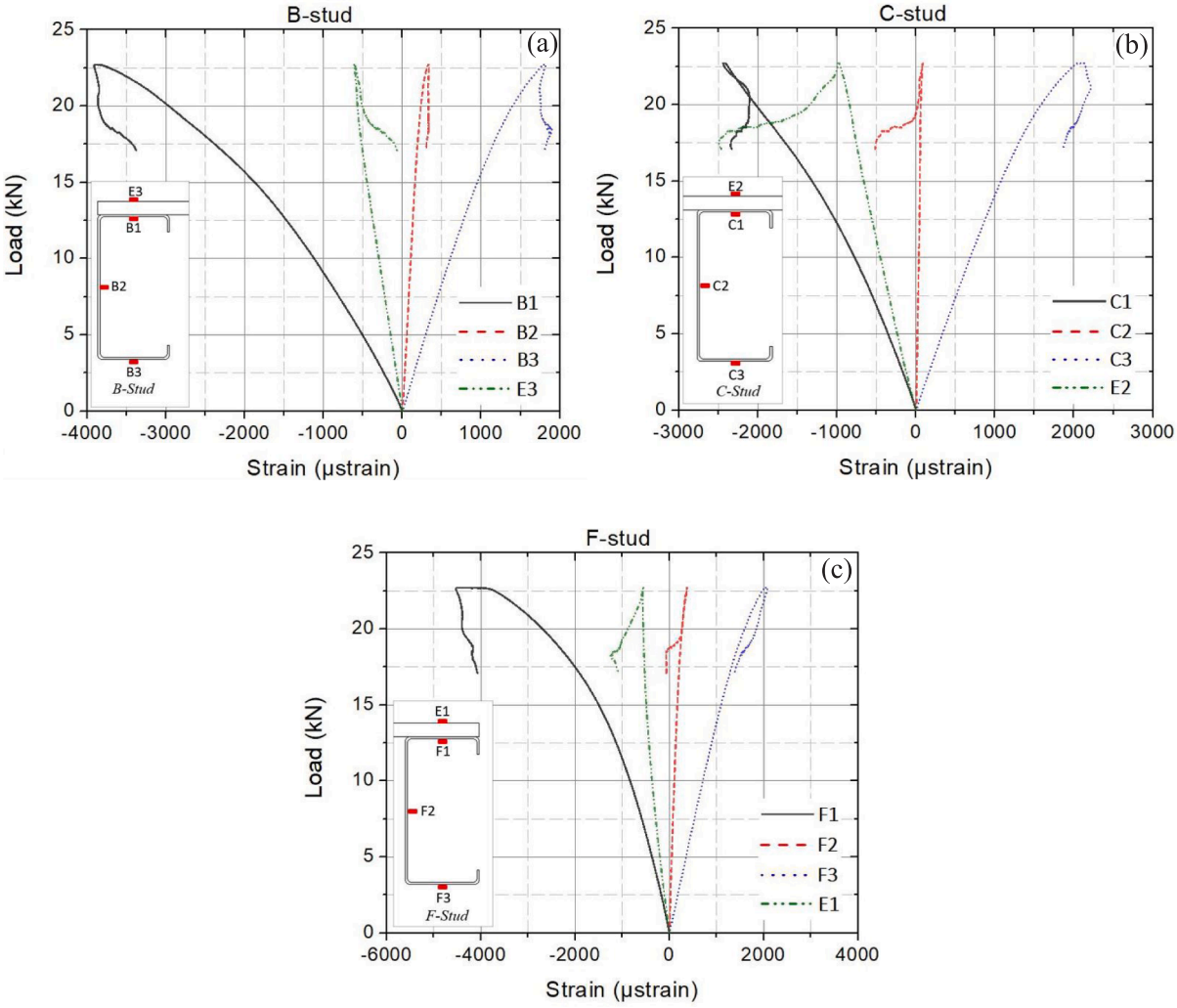

Fig. 31. Load–strain curves in studs and OSB for S300 specimen at various locations: (a) B-stud, (b) C-stud and (c) F-stud.

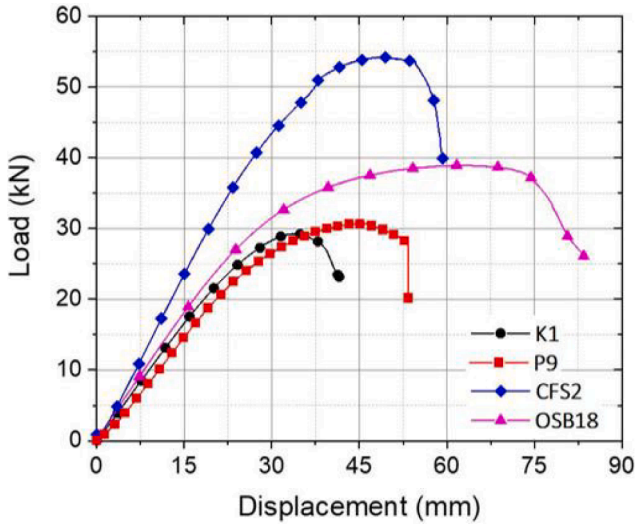

Fig. 32. Load–displacement responses of specimens P9 (9 mm plywood boards), OSB18 (18 mm OSB), CFS2 (2 mm CFS thickness) and key specimen K1.

specimens, although it is noted that the stiffness of P9 was marginally lower (by 10%). However, the failure mechanism was dramatically different, as illustrated in Fig. 35. In a failure mode more similar to that of OSB18, significant lateral and torsional deformations were observed, which were most pronounced in the boundary B-stud. In this case, this was mainly facilitated by the formation of a longitudinal crack in the plywood adjacent to the stud (Fig. 35b), although some localized plastic deformation also took place in the channel top flange around the screws. The strain gauge readings (Fig. 36) suggest good composite action in the initial stages of loading.

7.4. *Influence of the CFS thickness*

When increasing the thickness of the CFS elements (studs and tracks) in the key specimens from 1.2 mm to 2 mm, significant increases of 82% and 45% were obtained in the bending capacity and initial stiffness of the panel, respectively (Fig. 32 and Table 11). Pronounced lateral and torsional deformations were observed in the CFS2 specimen, accommodated by significant transverse bending in the OSB (Fig. 37a,b). All studs rotated towards the lip, consistent with the location of their shear centre, with the largest deflections and rotations observed in the boundary B-stud. As a result of the transverse bending stresses in the OSB, a longitudinal crack eventually formed in the middle of the panel, following the line of connectors (Fig. 37c). Minor damage was also

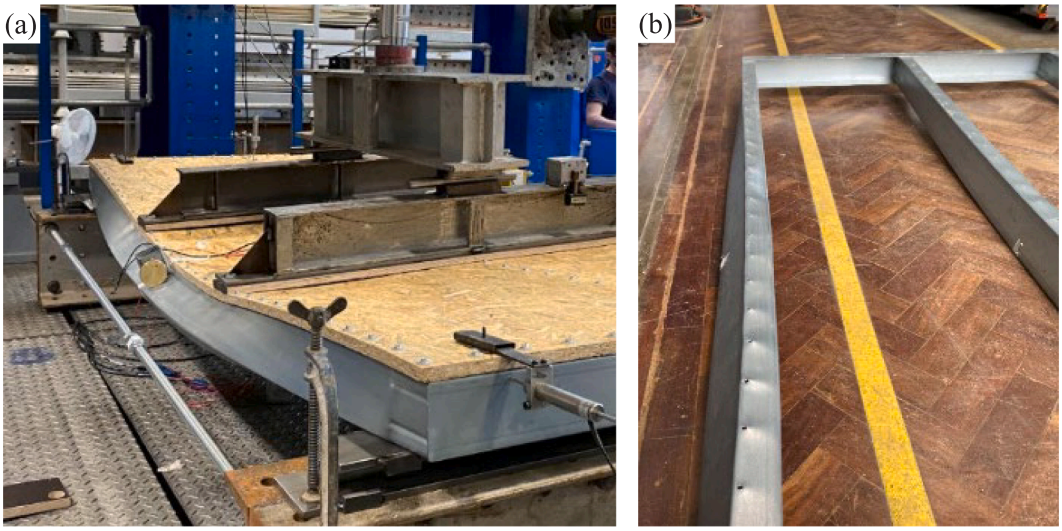

Fig. 33. Failure mode of specimen OSB18.

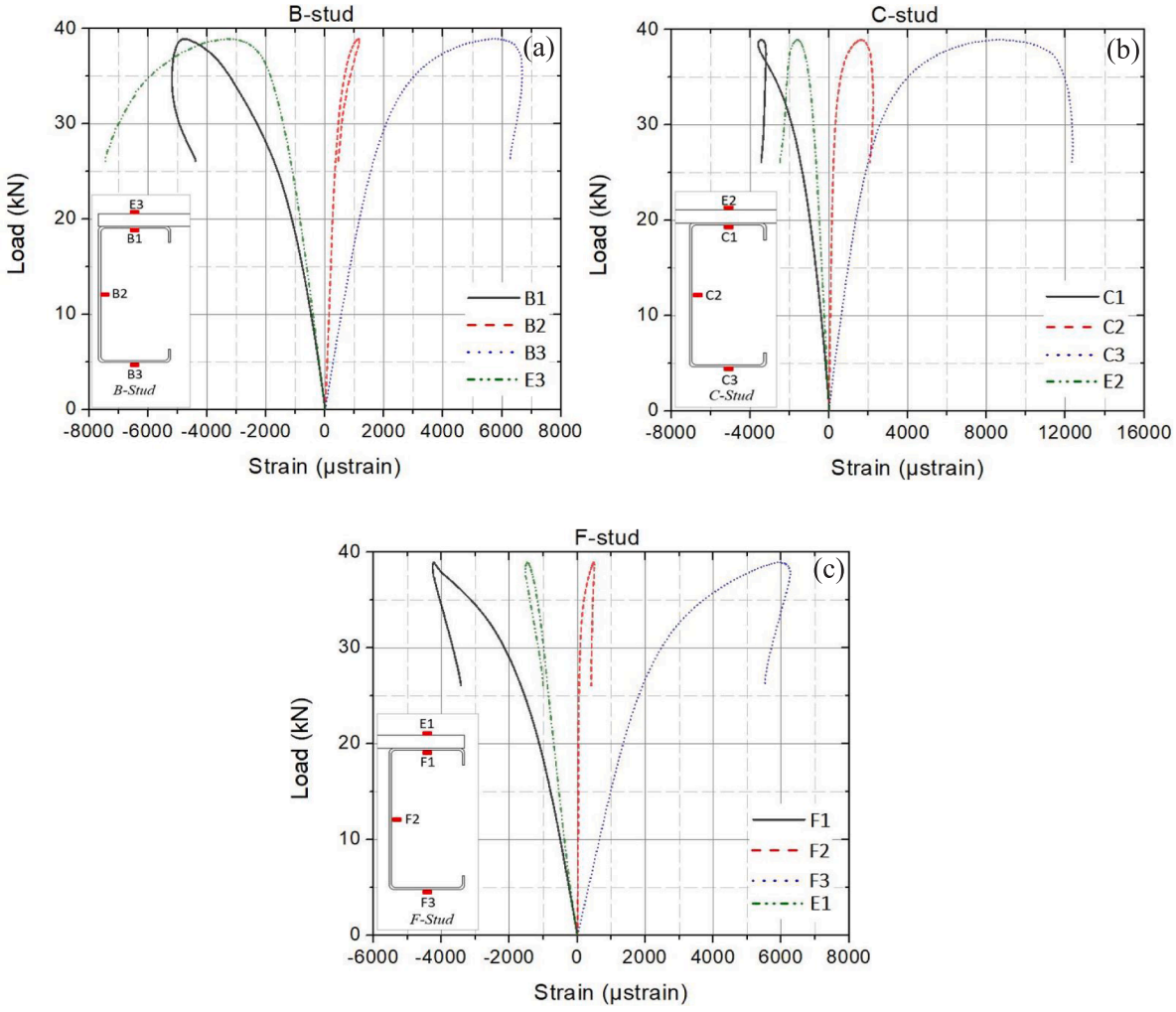

Fig. 34. Load–strain curves in studs and OSB for OSB18 specimen at various locations: (a) B-stud, (b) C-stud and (c) F-stud.

observed in the OSB adjacent to the F-stud, while longitudinal compressive stresses caused crushing of the OSB between connectors along the B-stud. In the later stages of loading a local buckle formed in the B-stud (Fig. 37c).

Fig. 38 presents the strain gauge readings in specimen CFS2 over the loading history. Full composite action was achieved in the initial stages of loading.

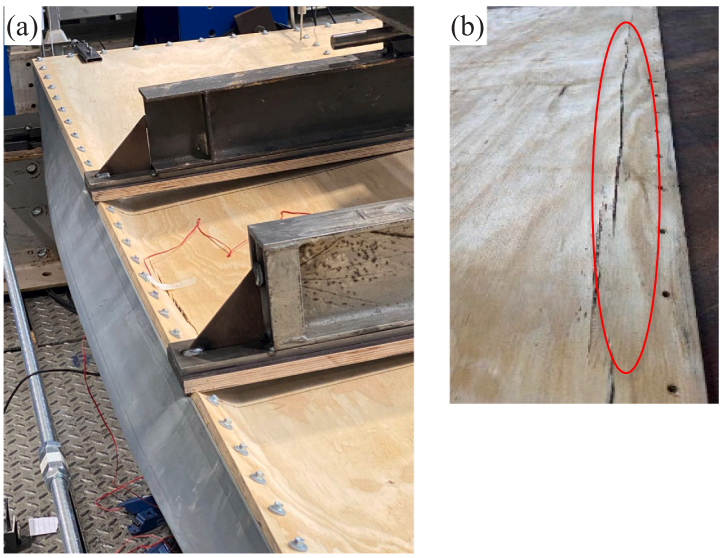

Fig. 35. Failure mode of specimen P9.

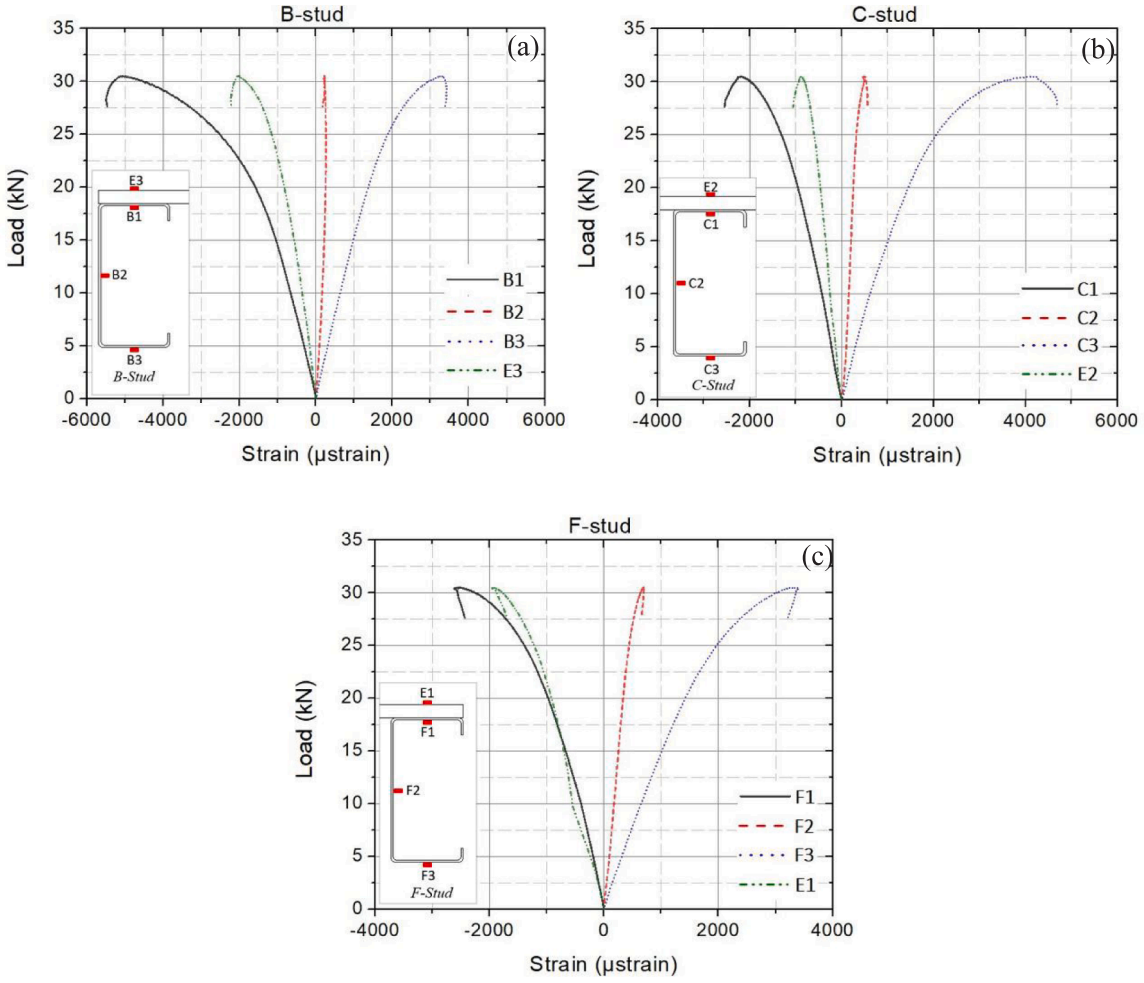

Fig. 36. Load–strain curves in studs and plywood for P9 specimen at various locations: (a) B-stud, (b) C-stud and (c) F-stud.

7.5. *Influence of various board configurations*

This section discusses the results obtained for the bare, unsheathed specimen (UB), the specimens with OSB sheathing on both sides (DB1 and DB2), and the specimen with single-sided OSB but reduced stud spacing (DR). Fig. 39 shows the load–displacement responses for all of these specimens and compares them to that of key specimen K1.

The test results of specimen UB reveal that removing the boards

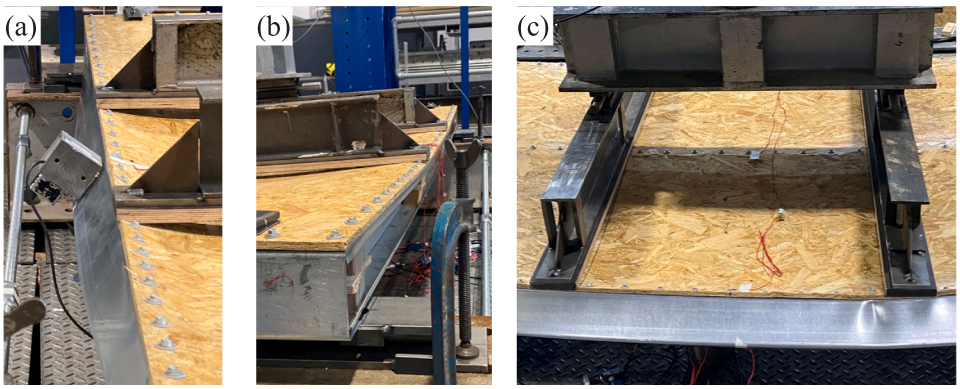

Fig. 37. Failure mode of CFS2 specimen.

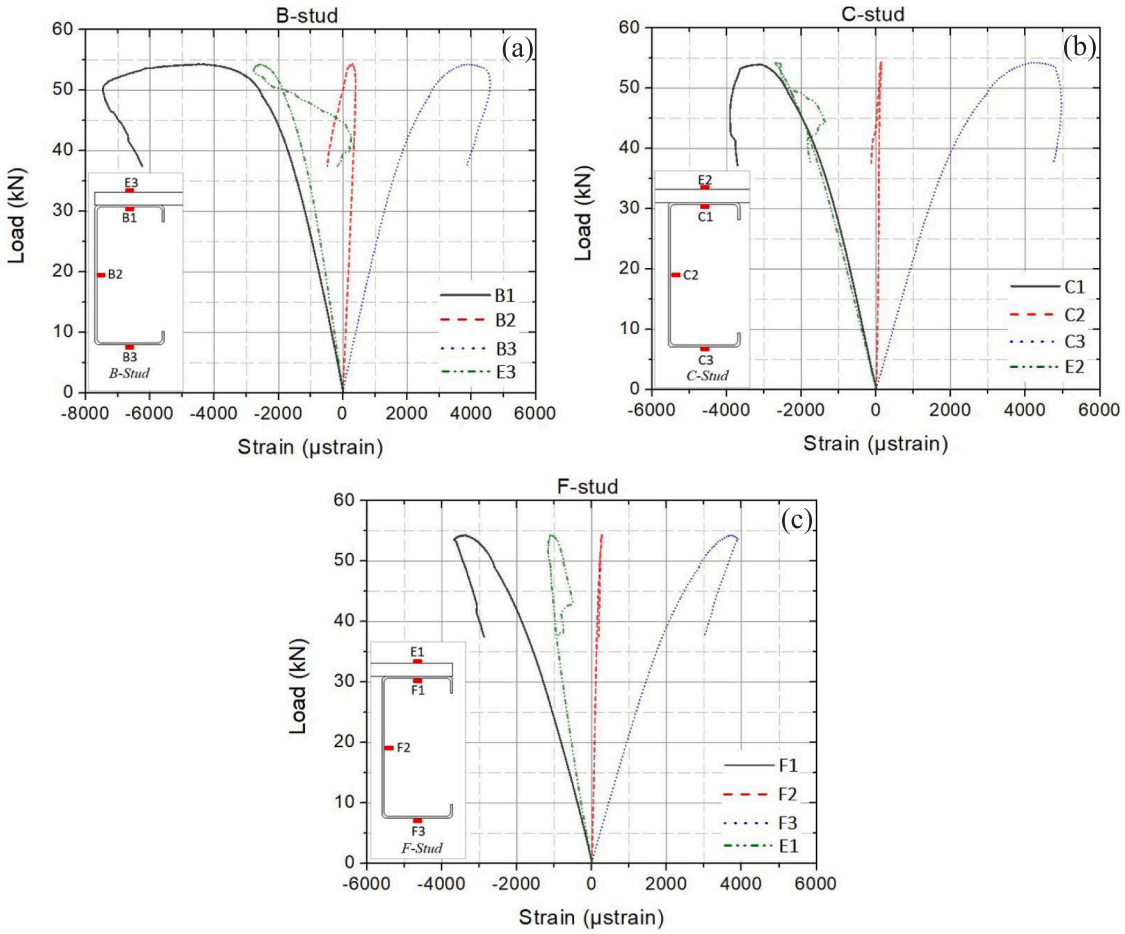

Fig. 38. Load–strain curves in studs and OSB for CFS2 specimen at various locations: (a) B-stud, (b) C-stud and (c) F-stud.

results in a striking reduction in both strength and stiffness of the panel. It is thereby noted that the loading beams still provided localized lateral restraint to the studs (Fig. 40a) and that, consequently, the capacity of studs unsupported along their full length would be even less. Nevertheless, the UB specimen illustrates the enormous benefits which can be obtained from accounting for the composite action between the studs and the boards. As illustrated in Fig. 40(a) and (b), the unsheathed system failed by lateral–torsional buckling of the studs, which interacted with local buckling in the final stages of loading.

Sheathing the studs with OSB on both sides (DB1 and DB2) was found to enhance the initial stiffness and strength of the stud wall by 45% and 16%, respectively, compared to the key specimen. Both double-sheathed specimens failed by local/distortional buckling of the CFS studs near mid-span, combined with crushing of the OSB on the compressive side (Fig. 41a,b). No damage was observed in the bottom OSB. As expected, the longitudinal twist rotations of the studs and the end slip values were significantly lower for the double-sheathed stud walls than for the single-sheathed specimens (see Tables 12 and 13). The strain gauge readings indicated full composite behaviour in the initial loading stages (Fig. 42).

When decreasing the stud spacing from 610 mm to 305 mm, while maintaining the number of studs in the panel at three, no statistically significant difference in bending capacity could be observed compared to the key specimens. The failure mechanism was also similar to that of

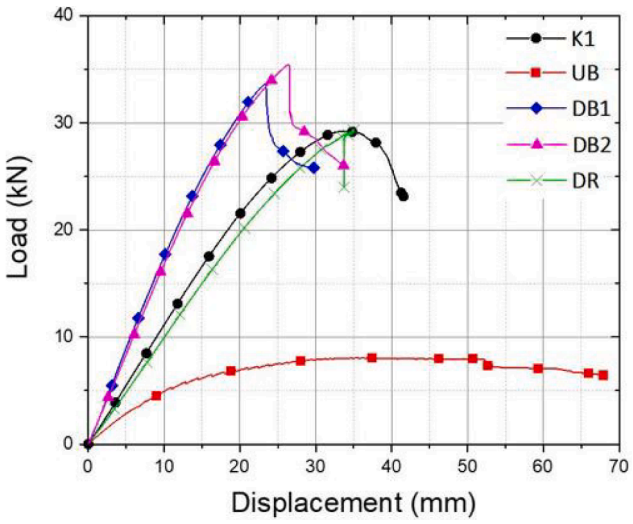

Fig. 39. Load–displacement responses of stud walls with different board configurations.

the key specimens and consisted of distortional buckling of the studs alongside crushing of the compressed OSB, as depicted in Fig. 43(a–c). The initial bending stiffness of the stud wall was slightly reduced by about 10% compared to the key specimens. The load–displacement response (Fig. 39) also showed a more sudden, brittle collapse. Fig. 44 presents the strain gauge readings, which indicate full composite behaviour.

7.6. Influence of secondary features

This section provides a discussion on the effects of three separate features on the panel behaviour: 1. the presence of a longitudinal seam in the panel (S), 2. the presence of noggins between the studs (N), and 3. the absence of top and bottom track sections (NT). While the latter is not a practically feasible configuration, it provides information on the implicit contributions of the track sections to the panel behaviour. Fig. 45 compares the load–deflection behaviour of these specimens to that of key specimen K1. The deflection was measured at the centre of the panel.

The S specimen had a longitudinal seam in the OSB which ran down the centre of the panel. The middle stud consequently featured a double row of screws, connecting the OSB on both sides of the stud. It is seen from Fig. 45 that the behaviour and capacity of the S specimen were quite similar to that of the key specimens. The failure mode consisted of distortional buckling of the studs and crushing of the OSB above (Fig. 46a). The ultimate bending capacity of the S panel was 31.3 kN m, which was slightly higher than that of K1 (29.2 kN m), but comparable to that of K2 (30.6 kN m). No statistically significant difference in initial stiffness was observed either. The strain gauge readings (see [45] for full results) indicated full composite action, as was already present in the key specimens, which featured the same screw spacing. End slip readings were comparable to those of the key specimens.

Specimen N contained a line of noggins at mid-span, which consisted of 100 × 58 × 1.2 channel sections, connected to the studs with 2 self-drilling screws in each flange. This did not alter the failure mode compared to the key specimens (Fig. 46b, c), and a comparable capacity of 31.1 kN m was obtained. However, the noggins had a beneficial influence on the initial bending stiffness of the panel, which increased by 18%. This can be attributed to the noggins largely preventing the stud (twist) rotations at mid-span, as illustrated by Fig. 47(a, b), which compare the rotations of the N and K2 specimens.

When testing the panel without the presence of the tracks, an initial bending stiffness similar to that of the key specimens was observed. However, the panel failed quite suddenly at a load 14% below the average capacity of the key specimens. Significant end rotations were observed in all studs before failure (Fig. 46d). Failure eventually occurred in the boundary F-stud (Fig. 46e) as a result of excessive twist rotations, made possible by the formation of a longitudinal fold line in the OSB adjacent to the connections under transverse bending stresses. This test illustrates the importance of the track sections in constraining the end rotations of the studs.

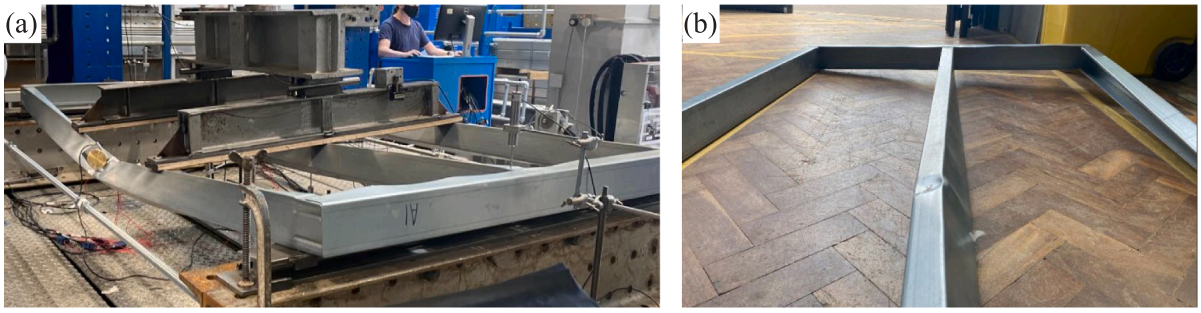

Fig. 40. Failure mode of unsheathed specimen UB.

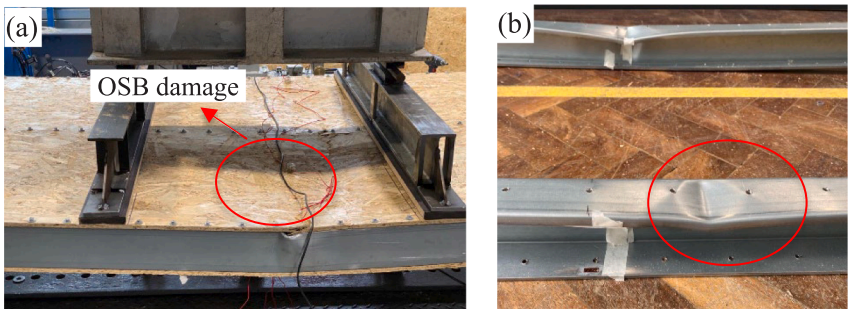

Fig. 41. Failure mode of double-sheathed specimen DB1.

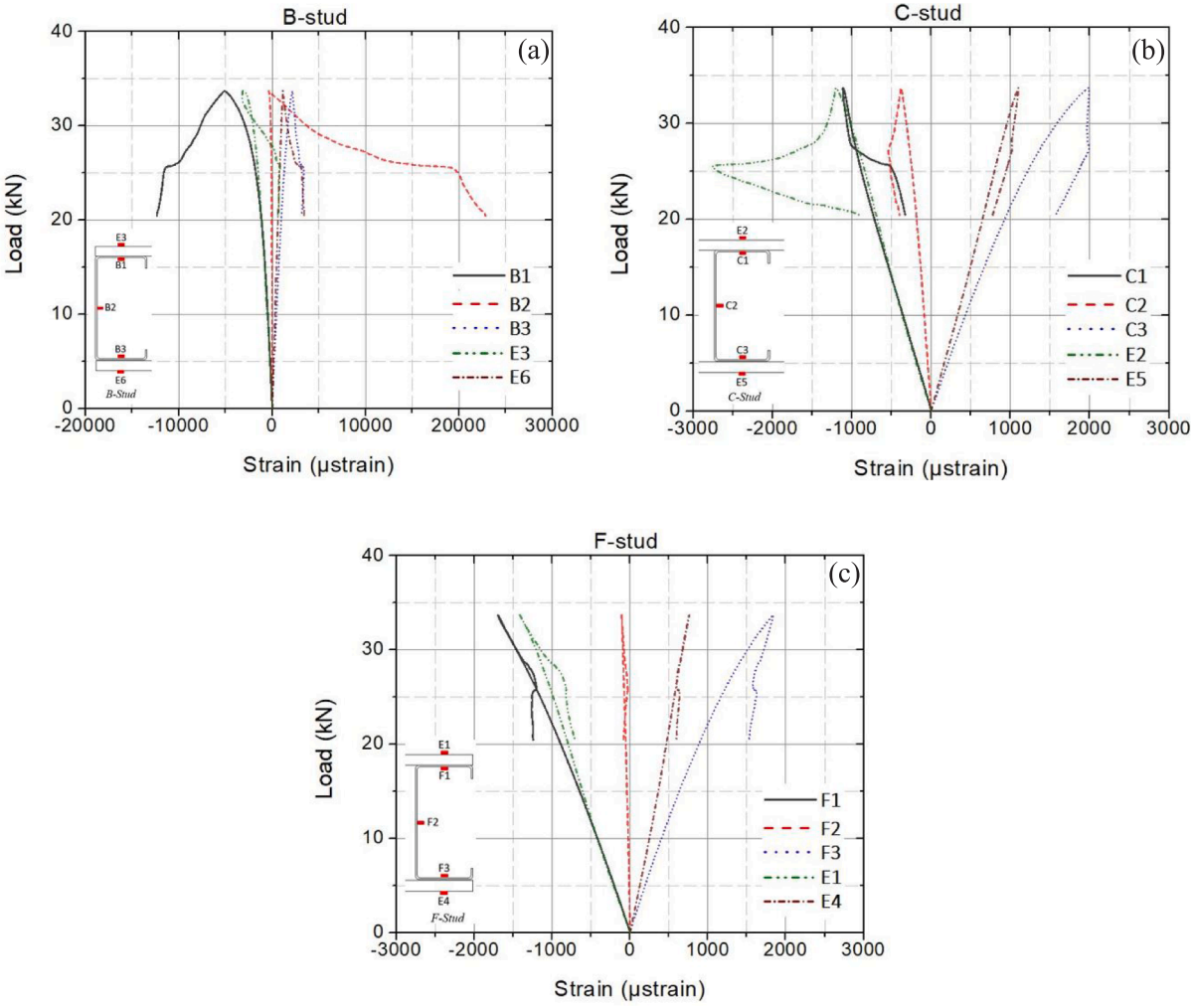

Fig. 42. Load–strain curves in studs and OSB for DB1 specimen at various locations: (a) B-stud, (b) C-stud and (c) F-stud.

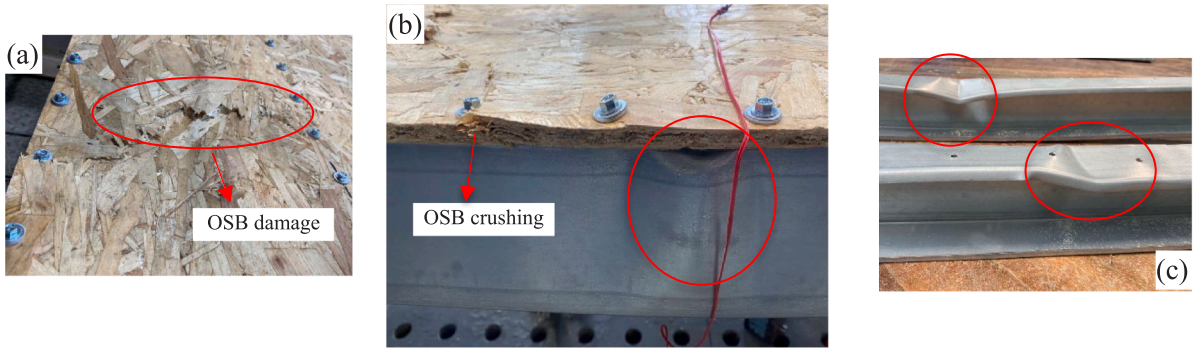

Fig. 43. Failure mode of DR specimen.

8. Summary and conclusions

This study investigated the out-of-plane bending behaviour and capacity of CFS stud wall panels sheathed with wood-based boards. A comprehensive experimental programme was conducted, which systematically varied the key design variables of the system, including the screw spacing, the thickness of the CFS studs, the thickness of the boards, the board material (OSB and plywood), the board configurations (unsheathed, single- and double-sheathed) and the presence/absence of secondary features (longitudinal seams, noggins and track sections). A series of material coupon tests, as well as push-out and pull-out connection tests, were also conducted.

The following conclusions were drawn from the experiments:

- The key specimens, featuring 9 mm thick OSB and 1.2 mm thick 100 × 50 × 10 lipped channels, failed by crushing of the OSB and distortional buckling of the studs. Full composite action between the two materials was observed for screw spacings of 75–100 mm. When

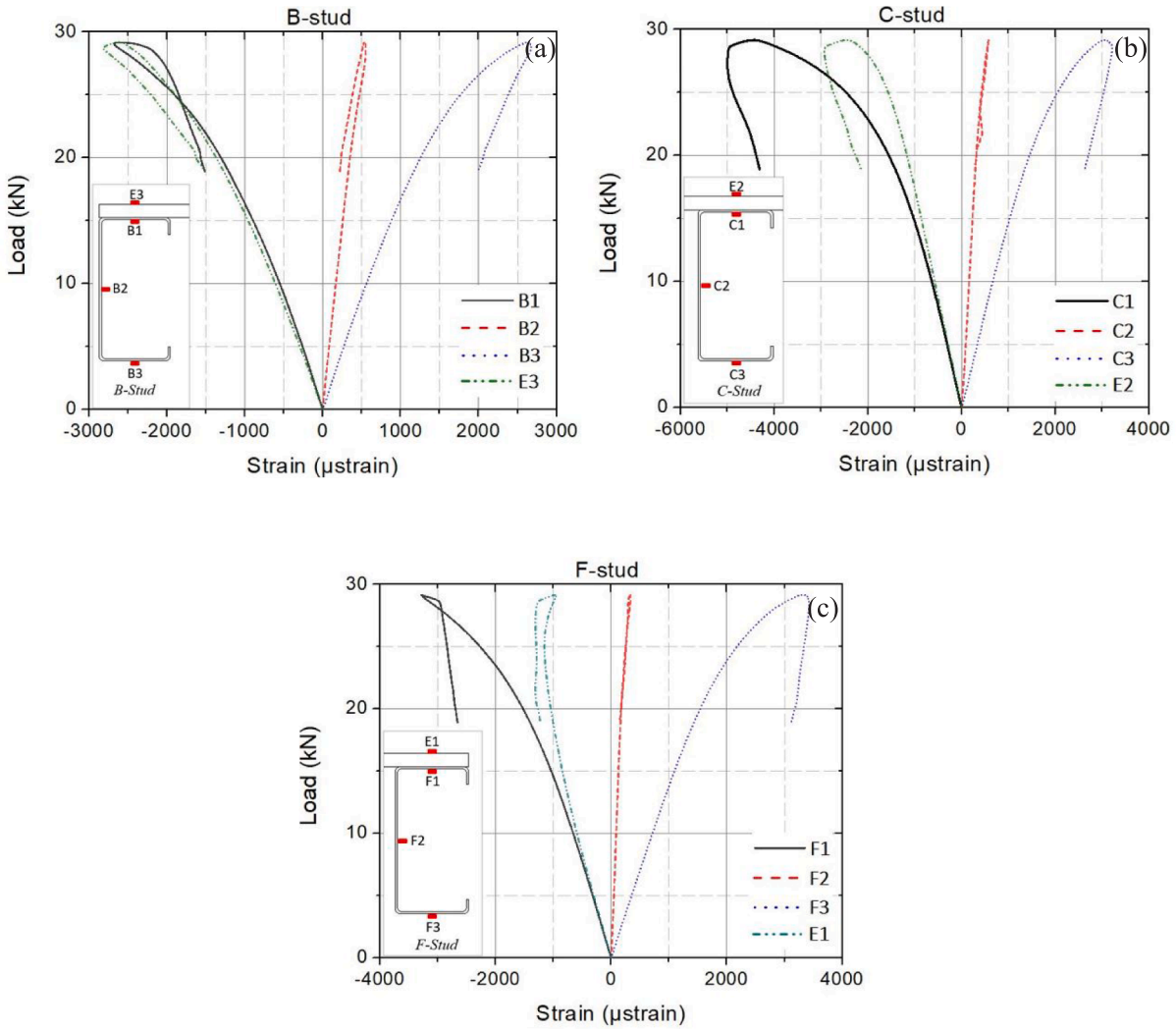

Fig. 44. Load–strain curves in studs and OSB for DR specimen at various locations: (a) B-stud, (b) C-stud and (c) F-stud.

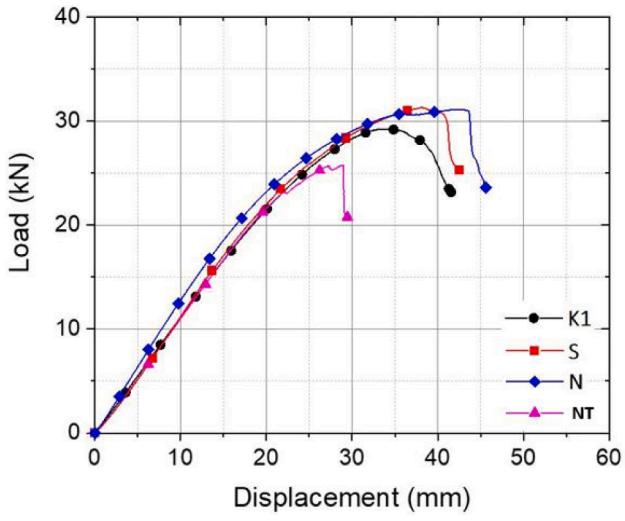

Fig. 45. Load–displacement responses of CFS stud walls, considering the effects of secondary features: seams, noggins and track sections.

increasing the screw spacing up to 300 mm, the failure mode remained the same but gradual reductions in bending capacity and stiffness were recorded. A reduced degree of composite action was also detected from increased end slip measurements and signs of bearing failure in the end screws.

- When doubling the thickness of the OSB to 18 mm, the bending capacity of the stud wall increased by 33%. Concurrently, the failure mechanism changed to torsion and lateral distortion of the studs, facilitated by localized deformations in the OSB-to-stud connections.
- A similar failure mechanism was observed when replacing the OSB by 9 mm thick plywood boards. The stud rotations were in this case exacerbated by longitudinal cracking of the plywood adjacent to the connectors. Compared to the key (OSB-clad) specimens, a similar bending capacity and slightly lower stiffness were observed.
- Increasing the CFS thickness from 1.2 mm to 2 mm significantly enhanced the bending capacity and stiffness of the stud wall (by 86% and 45%, respectively). Distortional buckling of the studs was replaced by lateral and torsional deformations, followed by longitudinal cracking of the board.
- Removing the OSB reduced the capacity of the system roughly by a factor of 3, and the stiffness by a factor of 2, illustrating the substantial benefits gained from composite action. On the other hand, the initial bending stiffness and the capacity of the stud wall with double-sheathed OSB were enhanced by 45% and 16% compared to the single-sheathed wall.

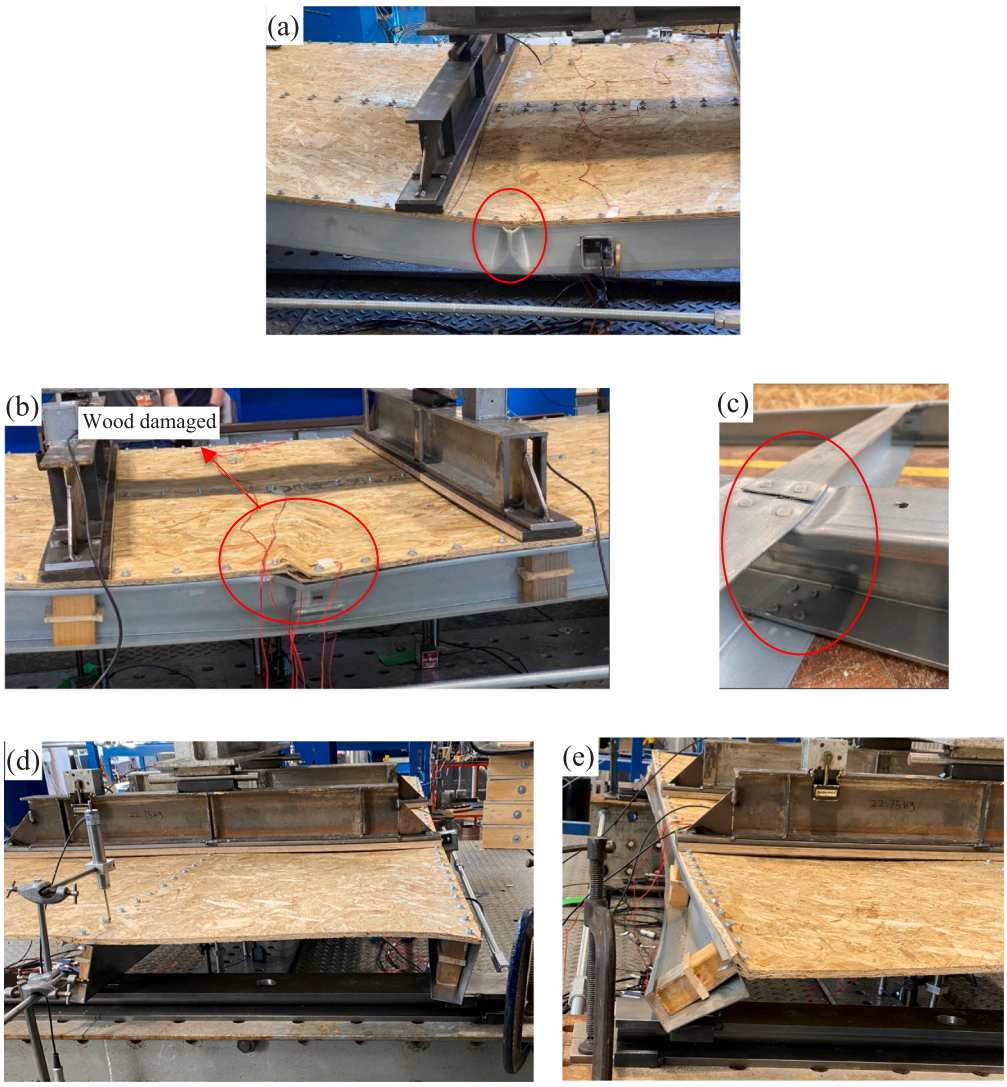

Fig. 46. Failure modes of (a) S specimen, (b, c) N specimen, and (d, e) NT specimen.

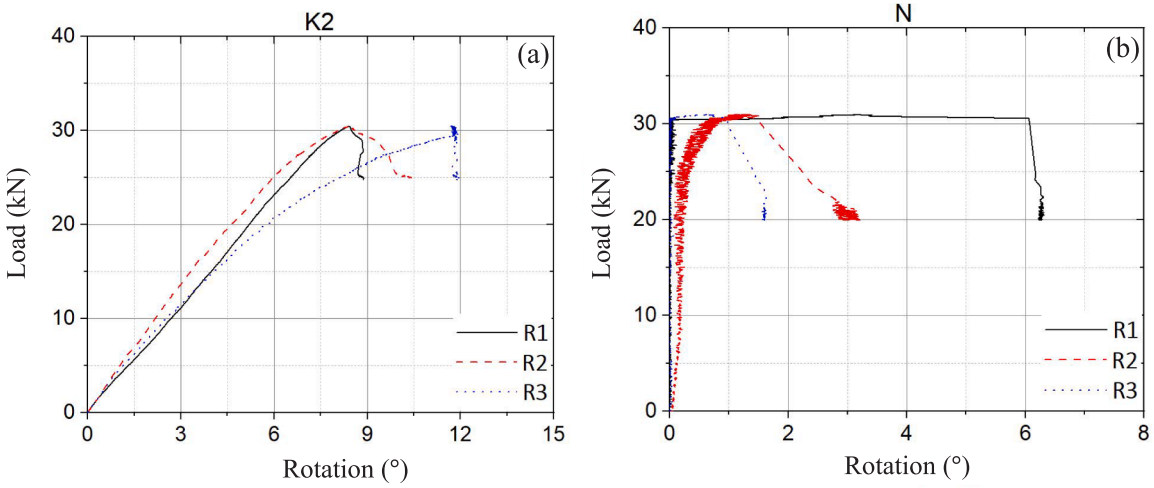

Fig. 47. Stud rotations about their longitudinal axis for: (a) K2, and (b) N specimens.

- The initial stiffness and the capacity of the stud wall remained almost unchanged when maintaining the number of studs in the panel but decreasing the stud spacing from 610 mm to 305 mm. However, failure became less ductile.
- The presence of a longitudinal seam did not have an important influence on the behaviour of the system. The presence of noggin elements improved the stiffness of the system by 18%, but did not noticeably affect the capacity.
- The track sections play an important role in preventing premature failure due to end rotations of the studs.

CRediT authorship contribution statement

Fatih Yilmaz: Writing – original draft, Visualization, Funding acquisition, Formal analysis, Data curation, Conceptualization. **Jurgen Becque:** Writing – review & editing, Validation, Supervision, Methodology, Conceptualization, Resources. **Seyed Mohammad Mojtabaei:** Writing – original draft, Visualization, Supervision, Methodology, Investigation, Data curation, Conceptualization. **Iman Hajirasouliha:** Supervision, Resources, Writing – review & editing, Conceptualization, Methodology.

Declaration of competing interest

The authors declare that they have no known competing financial interests or personal relationships that could have appeared to influence the work reported in this paper.

Data availability

Data will be made available on request.

Acknowledgement

The first author would like to thank the Turkish government, Ministry of National Education for supporting this project.

References

[1] J. Ye, I. Hajirasouliha, J. Becque, K. Pilakoutas, Development of more efficient cold-formed steel channel sections in bending, Thin-Walled Struct. 101 (2016) 1–13.
[2] I. Papargyriou, I. Hajirasouliha, More efficient design of CFS strap-braced frames under vertical and seismic loading, J. Construct. Steel Res. 185 (2021), 106886.
[3] S.E. Niari, B. Rafezy, K. Abedi, Seismic behavior of steel sheathed cold-formed steel shear wall: experimental investigation and numerical modeling, Thin-Walled Struct. 96 (2015) 337–347.
[4] B.W. Schafer, D. Ayhan, J. Leng, P. Liu, D. Padilla-Llano, K.D. Peterman, M. Stehman, S.G. Buonopane, M. Eatherton, R. Madsen, B. Manley, Seismic response and engineering of cold-formed steel framed buildings, in: Structures, Vol. 8, Elsevier, 2016, pp. 197–212.
[5] S. Shakeel, R. Landolfo, L. Fiorino, Behaviour factor evaluation of CFS shear walls with gypsum board sheathing according to FEMA P695 for Eurocodes, Thin-Walled Struct. 141 (2019) 194–207.
[6] M. Nithyadharan, V. Kalyanaraman, Behaviour of cold-formed steel shear wall panels under monotonic and reversed cyclic loading, Thin-Walled Struct. 60 (2012) 12–23.
[7] W.C. Gao, Y. Xiao, Seismic behavior of cold-formed steel frame shear walls sheathed with ply-bamboo panels, J. Construct. Steel Res. 132 (2017) 217–229.
[8] M. Accorti, N. Baldassino, R. Zandonini, F. Scavazza, C.A. Rogers, Reprint of response of CFS sheathed shear walls, in: Structures, Vol. 8, Elsevier, 2016, pp. 318–330.
[9] J. Ye, X. Wang, H. Jia, M. Zhao, Cyclic performance of cold-formed steel shear walls sheathed with double-layer wallboards on both sides, Thin-Walled Struct. 92 (2015) 146–159.
[10] J. Ye, X. Wang, M. Zhao, Experimental study on shear behavior of screw connections in CFS sheathing, J. Construct. Steel Res. 121 (2016) 1–12.
[11] E. Baran, C. Alica, Behavior of cold-formed steel wall panels under monotonic horizontal loading, J. Construct. Steel Res. 79 (2012) 1–8.
[12] W. Zhang, M. Mahdavian, C. Yu, Lateral strength and deflection of cold-formed steel shear walls using corrugated sheathing, J. Construct. Steel Res. 148 (2018) 399–408.
[13] J. Ye, X. Wang, H. Jia, M. Zhao, Cyclic performance of cold-formed steel shear walls sheathed with double-layer wallboards on both sides, Thin-Walled Struct. 92 (2015) 146–159.
[14] W. Mowrtage, N.H. Yel, B. Pekmezci, H.N. Atahan, Load carrying capacity enhancement of cold formed steel walls using shotcreted steel sheets, Thin-Walled Struct. 60 (2012) 145–153.
[15] F. Yilmaz, S.M. Mojtabaei, I. Hajirasouliha, J. Becque, Behaviour and performance of OSB-sheathed cold-formed steel stud wall panels under combined vertical and seismic loading, Thin-Walled Struct. 183 (2023) (2023), 110419.
[16] I. Rouaz, N. Bourahla, S. Kechidi, Numerical evaluation of shear strength of CFS shear wall panels for different height-to-width ratios, J. Mater. Eng. Struct. (JMES) 5 (4) (2018) 399–417.
[17] Z. Xie, W. Yan, C. Yu, T. Mu, L. Song, Experimental investigation of cold-formed steel shear walls with self-piercing riveted connections, Thin-Walled Struct. 131 (2018) 1–15.
[18] L. Fiorino, T. Pali, B. Bucciero, V. Macillo, M.T. Terracciano, R. Landolfo, Experimental study on screwed connections for sheathed CFS structures with gypsum or cement based panels, Thin-Walled Struct. 116 (2017) 234–249.
[19] J. DaBreo, N. Balh, C. Ong-Tone, C.A. Rogers, Steel sheathed cold-formed steel framed shear walls subjected to lateral and gravity loading, Thin-Walled Struct. 74 (2014) 232–245.
[20] L. Fiorino, T. Pali, R. Landolfo, Out-of-plane seismic design by testing of non-structural lightweight steel drywall partition walls, Thin-Walled Struct. 130 (2018) 213–230.
[21] S. Selvaraj, M. Madhavan, Investigation on sheathing effect and failure modes of gypsum sheathed cold-formed steel wall panels subjected to bending, in: Structures, Vol. 17, Elsevier, 2019, pp. 87–101.
[22] B.W. Schafer, Sheathing braced design of wall studs, in: AISI-Specifications for the Design of Cold-Formed Steel Structural Members, Vol. 115, 2013.
[23] S. Selvaraj, M. Madhavan, Studies on cold-formed steel stud panels with gypsum sheathing subjected to out-of-plane bending, J. Struct. Eng. 144 (9) (2018), 04018136.
[24] S. Selvaraj, M. Madhavan, Structural behaviour and design of plywood sheathed cold-formed steel wall systems subjected to out of plane loading, J. Construct. Steel Res. 166 (2020), 105888.
[25] AISI. (American Iron and Steel Institute), North American Cold-Formed Steel Specification for the Design of Cold-Formed Steel Structural Members, AISI-S100–16C, Washington, DC, 2016.
[26] J. Ye, X. Wang, M. Zhao, Experimental study on shear behavior of screw connections in CFS sheathing, J. Construct. Steel Res. 121 (2016) 1–12.
[27] Z.G. Huang, Y.J. Wang, M.Z. Su, L. Shen, Study on restoring force model of cold-formed steel wall panels and simplified seismic response analysis method of residential buildings, China Civ. Eng. J. 45 (2012) 26–34.
[28] O.K. Dowell, F. Seible, E.L. Wilson, Pivot hysteresis model for reinforced concrete members, ACI Struct. J. 95 (1998) 607–617.
[29] L. Fiorino, T. Pali, B. Bucciero, V. Macillo, M.T. Terracciano, R. Landolfo, Experimental study on screwed connections for sheathed CFS structures with gypsum or cement based panels, Thin-Walled Struct. 116 (2017) 234–249.
[30] CEN, EN 1995-1-1: Eurocode 5 - Design of Timber Structures - General - Common Rules and Rules for Buildings, Vol. 144, European Committee for Standardization, 2004, pp. 39–43.
[31] N. Ringas, Y. Huang, J. Becque, Fastener behaviour in sheathed light-gauge steel stud walls under cyclic and monotonic actions, ce/papers 4 (2–4) (2021) 517–524.
[32] P. Kyvelou, L. Gardner, D.A. Nethercot, Testing and analysis of composite cold-formed steel and wood-based flooring systems, J. Struct. Eng. 143 (11) (2017), 04017146.
[33] P. Kyvelou, L. Gardner, D.A. Nethercot, Finite element modelling of composite cold-formed steel flooring systems, Eng. Struct. 158 (2018) 28–42.
[34] D. Karki, S. Al-Hunaity, H. Far, A. Saleh, Composite connections between CFS beams and plywood panels for flooring systems: Testing and analysis, in: Structures, Vol. 40, Elsevier, 2022, pp. 771–785.
[35] European Committee for Standardization (CEN), Oriented Strand Boards (OSB). Definitions, Classification and Specifications: EN 300, CEN, Brussels, 2006.
[36] European Committee for Standardization (CEN), Plywood Specifications: EN 636, CEN, Brussels, 2012.
[37] EN ISO 6892-1:2009, Metallic Materials – Tensile Testing – Part 1: Method of Test at Room Temperature, International Organization for Standardization.
[38] Y. Huang, B. Young, The art of coupon tests, J. Construct. Steel Res. 96 (2014) 159–175.
[39] BS EN 789:2004, Timber Structures. Test Methods. Determination of Mechanical Properties of Wood Based Panels, 2004.
[40] A. Neut, The interaction of local buckling and column failure of thin-walled compression members, in: Applied Mechanics, Springer, Berlin, Heidelberg, 1969, pp. 389–399.
[41] J. Becque, Local-overall interaction buckling of inelastic columns: A numerical study of the inelastic Van der Neut column, Thin-Walled Struct. 81 (2014) 101–107.
[42] M. Hasanali, S.M. Mojtabaei, G.C. Clifton, I. Hajirasouliha, S. Torabian, J.B.P. Lim, Capacity and design of cold-formed steel warping-restrained beam–column elements, J. Construct. Steel Res. 190 (2022), 107139.

[43] F. Öztürk, S.M. Mojtabaei, M. Şentürk, S. Pul, I. Hajirasouliha, Buckling behaviour of cold-formed steel sigma and lipped channel beam–column members, Thin-Walled Struct. 173 (2022), 108963.
[44] F.J. Meza, J. Becque, I. Hajirasouliha, Experimental study of cold-formed steel built-up columns, Thin-Walled Struct. 149 (2020), 106291.
[45] F. Yilmaz, The Behaviour of Sheathed Cold-Formed Steel Stud Wall Systems under In-Plane and Out-of-Plane Loading (Doctoral dissertation), University of Sheffield, Sheffield, 2022.